

Structural basis of circularly permuted group II intron self-splicing

Received: 26 March 2024

Accepted: 3 January 2025

Published online: 31 January 2025

 Check for updates

Liu Wang  ^{1,2,6}, Jiahao Xie ^{1,3,6}, Chong Zhang ^{1,6}, Jian Zou ¹, Zirui Huang ¹, Sitong Shang ⁴, Xingyu Chen ¹, Yang Yang ^{1,5}, Jianquan Liu ⁴, Haohao Dong  ¹, Dingming Huang  ^{1,2}✉ & Zhaoming Su  ¹✉

Circularly permuted group II introns (CP introns) consist of rearranged structural domains separated by two tethered exons, generating branched introns and circular exons via back-splicing. Structural and mechanistic understanding of circular RNA (circRNA) generation by CP introns remains elusive. We resolve cryo-electron microscopy structures of a natural CP intron in different states during back-splicing at a resolution of 2.5–2.9 Å. Domain 6 (D6) undergoes a conformational change of 65° after branching, to facilitate 3'-exon recognition and circularization. Previously unseen tertiary interactions compact the catalytic triad and D6 for splicing without protein, whereas a metal ion, M₃₅, is observed to stabilize the 5'-exon during splicing. While these unique features were not observed in canonical group II introns and spliceosomes, they are common in CP introns, as demonstrated by the cryo-EM structure of another CP intron discovered by comparative genomics analysis. Our results elucidate the mechanism of CP intron back-splicing dynamics, with potential applications in circRNA research and therapeutics.

Group II introns are large structured RNA enzymes ranging from 400–900 nucleotides that carry out two transesterification reactions to self-splice and ligate the exons^{1,2}. Most introns also encode a maturase protein with helicase and reverse transcriptase activity that facilitates the reverse splicing process, known as retrotransposition, to invade DNA as selfish mobile genetic elements^{2,3}. This probably accounts for their widespread distribution in prokaryotes, mitochondria and chloroplasts of fungi, algae, plants and lower eukaryotes^{4,5}. The structural and mechanistic similarities between group II introns and spliceosomes suggest that they are likely ancestors of nuclear pre-mRNA introns and spliceosomes^{6,7}.

Group II introns consist of six conserved structural domains (D1–D6) from the 5' to 3' end (Extended Data Fig. 1a)^{1,4}. Starting from the 5' end, the 5'-exon and 5'-splice site (5'-SS) are followed by the

intron's largest D1 domain, which serves as a structural scaffold and contains exon-binding sites (EBSs). D2 and D3 interact extensively with D1, D5 and D6 to organize the catalytic core and position D6 for catalysis. Importantly, the conserved junction between D2 and D3 (J2/3) is essential to catalytic site formation in D5. D4 carries the intron-encoded protein (IEP) that facilitates the forward and reverse splicing processes. D5 is the most conserved domain, analogous to U6 small nuclear RNA (snRNA) in spliceosomes, and contains the catalytic triad stabilized by a two-nucleotide bulge and J2/3 to shape the intact catalytic core. D6 contains the conserved bulged A to cleave the 5'-SS and form the lariat with a 2'-5' phosphodiester linkage. In the second reaction, the 3'-SS of the 3'-exon is attacked by the 5'-exon to remove the lariat intron and ligate the exons. D6 undergoes large conformational change assisted by IEP in both forward and reverse splicing^{8,9}.

¹The State Key Laboratory of Biotherapy, National Clinical Research Center for Geriatrics, West China Hospital; The State Key Laboratory of Oral Diseases, National Clinical Research Center for Oral Diseases, National Center for Stomatology, West China Hospital of Stomatology, Sichuan University, Chengdu, China. ²Department of Cariology and Endodontics, West China Hospital of Stomatology, Sichuan University, Chengdu, China. ³Mingle Scope (Chengdu), Chengdu, China. ⁴The Key Laboratory for Bio-resources and Eco-environment of Ministry of Education, College of Life Sciences, Sichuan University, Chengdu, China. ⁵Department of Prosthodontics, West China Hospital of Stomatology, Sichuan University, Chengdu, China. ⁶These authors contributed equally: Liu Wang, Jiahao Xie, Chong Zhang. ✉e-mail: dingminghuang@163.com; zsu@wchscu.cn

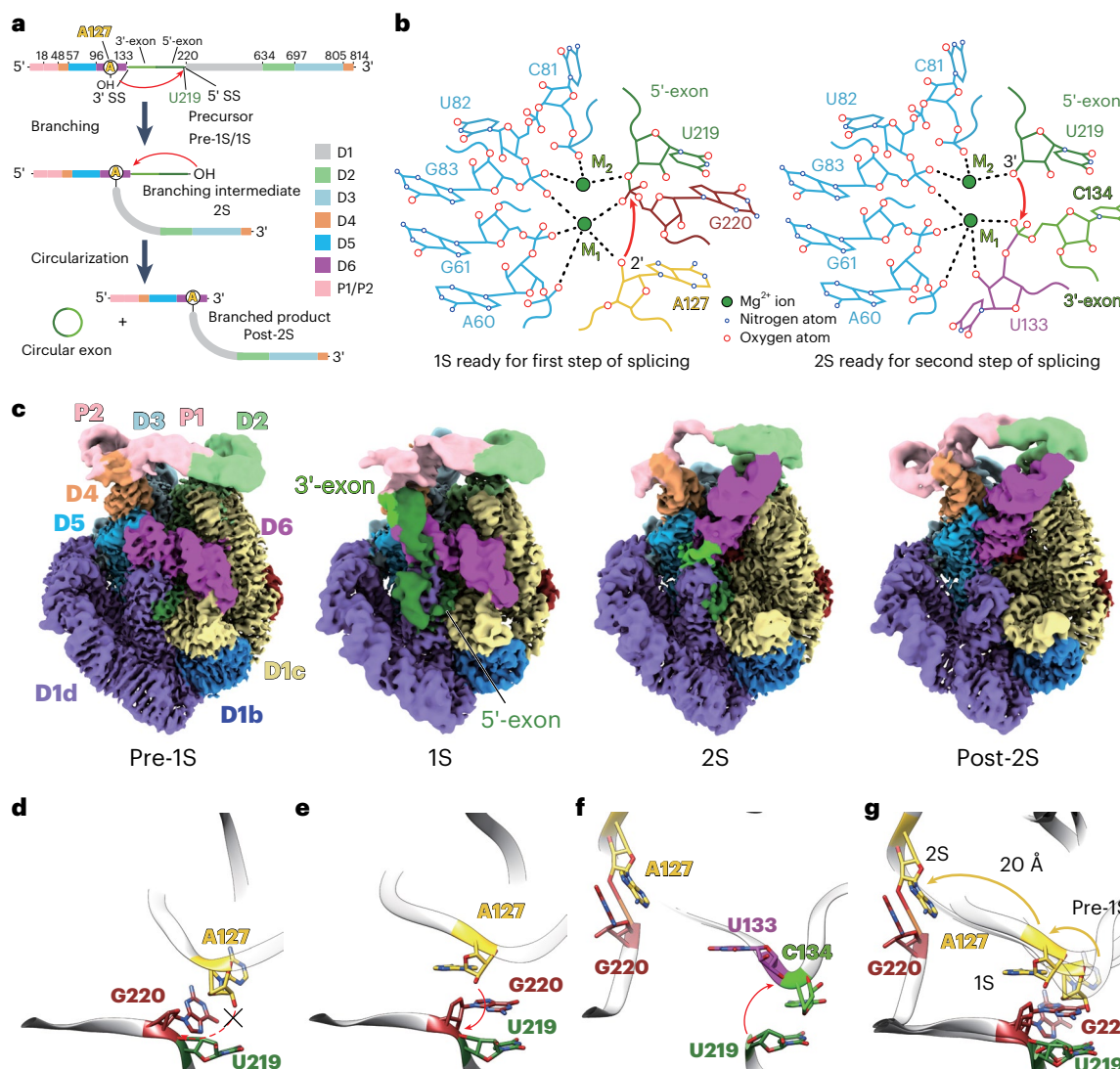


Fig. 1 | Cryo-EM structures of Cte1 intron self-splicing process. **a**, Schematic view of CP group II intron self-splicing to generate circular exon product. **b**, Schematic views of the catalytic site organized for the first (1S) and second (2S) step of the splicing reaction. **c**, Cryo-EM structures of four different states: pre-1S, 1S, 2S and post-2S during the Cte1 intron splicing process. **d–f**, Arrangement of

A127, U219 and G220 in pre-1S (**d**), 1S ready for branching (**e**) and 2S ready for circularization (**f**). **g**, Conformational changes of bulged A127 and G220 from pre-1S through 1S to 2S. Black dashed lines indicate metal ion coordination, red arrows indicate nucleophilic attacks, gold arrows indicate conformational changes of A127 and G220 from pre-1S through 1S to 2S.

Permutation occurs in DNA, RNA and protein that alters their sequence order while retaining their function and structure¹⁰. Circular permutation is the most common rearrangement, which swaps the sequence order by joining the original termini and introducing a new cleavage site, resulting in new termini^{11,12}. CP group I and II introns have been artificially designed to produce circular RNAs (circRNAs)^{13,14}. CircRNAs are increasingly recognized for their important role in regulating fundamental biological processes and their potential applications in therapeutics, such as vaccines^{15,16}. Recently, natural CP group II introns have been discovered in bacterial chromosomes and plasmids, with D5, D6 and 3'-exon swapping to the 5' end of the 5'-exon, analogous to those previously designed^{14,17}. Two steps of splicing reactions analogous to canonical group II introns are carried out in the absence of protein, as D4 lacks a coding region. In the first step, the bulged A in D6 cleaves the 5'-SS to form a branching intermediate (BI) containing both exons and the 3'-SS, which is subsequently cleaved by the 5'-exon in the second step to remove the branched product (BP) and generate the circular exons (Fig. 1a). Although the circular exon lengths generated by the identified natural CP group II introns were generally below

100 nucleotides¹⁷, a recent study reported the production of circRNAs longer than 700 nucleotides, which could be robustly and persistently translated into proteins, including those from pathogens, to trigger immune responses¹⁸. Despite the promising therapeutic applications of circRNA vaccines produced by CP intron catalysis, structural insights into the CP introns remain elusive, precluding our mechanistic understanding of the dynamic process underlying circRNA production.

Single-particle cryo-EM has become increasingly useful for studying structures and the dynamics of large ribozymes undergoing catalysis in the absence of proteins^{19–22}. In this work, we employed cryo-EM to investigate the catalytic process of a natural CP group II intron previously identified from *Comamonas testosteroni* KF-1 (Cte1, 814 nucleotides)¹⁷. We defined conformations organized to carry out the first and second steps of back-splicing as 1S and 2S (Fig. 1b). Conformations before and after these states are denoted by ‘pre-’ and ‘post-’. Four structures revealing different states of pre-1S, 1S, 2S and post-2S were determined at resolutions of 2.5, 2.9, 2.6 and 2.8 Å, respectively (Fig. 1c).

The 5'-SS is in close proximity to bulged A127 and ready for cleavage in the 1S state upon binding to EBS1 (nucleotides 540–545), which

is unexpectedly stabilized by a major groove interaction involving three base triples from adjacent nucleotides in the same EBS loop (nucleotides 535–537). In pre-1S, bulged A127 flips away from the 5'-SS while D6 maintains similar position as in 1S. In the 2S state after branching, a 65° conformational change of D6 containing the branched 2'-5' phosphodiester linkage (A127-G220) facilitates the rearrangement of 5'-exon-IBS3 base pairing in 1S to the 3'-exon docking in 2S, recognized by a two-nucleotide EBS3 (C538 and G539). After circRNA release, the EBS loop stabilizes through local rearrangements, forming two internal base triples. The 3'-SS coordinates with a network of interactions, resembling the lariat forms of canonical group II introns poised for transposition. Unexpected tertiary interactions are observed in the peripheral regions to maintain the catalytic core as compact for splicing without IEP. A total of 60 metal ions has been identified in these structures, with two metal ions consistently found in the catalytic site directly participating in the splicing process, suggesting that both reactions proceed through the conventional two-metal-ion mechanism²³. A previously unreported metal ion, M₃₅, was identified near the conserved heteronuclear metal ion center, to coordinate with the 5'-exon for both splicing reactions.

While these unique findings of exon interactions, 3'-SS recognition and M₃₅ were not observed in canonical group II introns and spliceosomes, they have been confirmed to be conserved in CP group II introns by cryo-EM structural analysis of another CP intron in *Paracandidimonas lactea* (*Pla*), discovered by comparative genomics analysis. Collectively, these structures illustrate snapshots of the dynamic back-splicing process of natural CP group II introns and elucidate mechanistic insights into circular exon generation that are conserved and unique to CP group II introns. This study provides a structural basis for circRNA production, with potential applications in research and therapeutics.

Results

Cryo-EM structures of different states in *Cte1* splicing

The *Cte1* RNA construct was prepared by in vitro transcription (IVT), during which the catalytic reactions have already occurred after cotranscriptional folding in the presence of Mg²⁺ (Extended Data Fig. 1b)^{20,24,25}. The BI band was not observed in denatured gel electrophoresis, suggesting that both the first and second catalytic reactions occurred almost simultaneously, analogous to canonical group II intron splicing^{8,26}. To capture the branching (1S) and ligation (2S) states, we purified the pre-RNA and replaced Mg²⁺ with Ca²⁺ in catalytic reactions that have previously been shown to inhibit splicing^{8,26–28}. Denaturing gel electrophoresis showed the accumulation of BI as the splicing reaction proceeded, and the 5-min and 4-h time points were subjected to cryo-EM analysis (Extended Data Fig. 1c). Three-dimensional (3D) classification and refinement yielded reconstructions at 2.5 Å, 2.9 Å and 2.6 Å resolution, representing pre-1S, 1S and 2S states, respectively (Fig. 1c and Extended Data Fig. 2). Cryo-EM analysis of the IVT product yielded another reconstruction of the branched product at 2.8 Å resolution, corresponding to the post-2S state with circular exons released as opposed to 2S with exons bound (Fig. 1c, Table 1 and Extended Data Fig. 3).

Different states are designated based on the connection of 5'-SS to IBS1 (pre-1S and 1S), the presence of both EBS1–IBS1 and EBS3–IBS3 ready for exon ligation (2S), and the A127-G220 2'-5' phosphodiester linkage density (2S and post-2S) (Extended Data Fig. 4). In the pre-1S and 1S structures, the D6 helix points toward D1c, positioning the 2'-OH of bulged A127 in close proximity to the scissile phosphate at the 5'-SS. The 1S structure is distinguished from the pre-1S because bulged A127 in 1S is ready to cleave the docked 5'-exon (Fig. 1d–e and Extended Data Fig. 4a,b). The 2S structure has the A127-G220 2'-5' phosphodiester linkage and D6 pointing towards D2, translocated 65° away from pre-1S and 1S conformations (Fig. 1f–g and Extended Data Fig. 4c). The post-2S adopts a conformation nearly identical to that of 2S, except for the missing density of 5'- and 3'-exons (Extended Data Fig. 4d).

Conformational dynamics of helix D6 and branchpoint A127

The *Cte1* intron consists of novel P1 and P2 domains at the 5' end, followed by D5 and D6 that establish the catalytic core, the intervening 3'- and 5'-exons awaiting excision and the scaffold D1–D3, with D4 at the 3' end forming a closing stem (Fig. 1a and Extended Data Fig. 5a). D5 contains the conserved catalytic triad (A60, G61, C62) and two-nucleotide bulge that collectively form a catalytic triplex core homologous to the spliceosome U2/U6 small nuclear RNA^{1,29}. Multiple long-range tertiary interactions, denoted by Greek letters, are identified between D5 and D1 ($\psi'-\phi$, $\lambda'-\lambda$, $\zeta'-\zeta$)^{30,31}, D3 ($\kappa'-\kappa$, $\mu'-\mu$) and D4 ($\phi'-\phi$), to organize the catalytic core^{32,33}, which are consistent with those previously observed in canonical group II introns (Extended Data Fig. 5b–h)^{9,25,34,35}. D6 is downstream of D5, containing the branchpoint A127 and a few previously identified tertiary interactions with D1 ($\pi'-\pi$) and D2 ($\eta'-\eta$, $\gamma'-\gamma$), which facilitates D6 dynamics between different catalytic states (Extended Data Fig. 5i–k)^{8,9,34,36}.

Cryo-EM structures reveal substantial conformational changes and local shifts from branching to exon ligation of *Cte1* intron back-splicing. The branching helix D6 has previously been reported to undergo ~90° translocation, enabled by IEP, between two transesterification reactions in both self-splicing and transposition processes^{8,9}. In the *Cte1* intron, the conformational change of D6 between the first and second splicing reaction is mostly facilitated by the η' interaction motif of the D6 terminal T-loop. In pre-1S and 1S, we observed a tertiary interaction between the D6 T-loop and the D1c terminal loop (later defined as the B' interaction motif), anchored by a G111-A451 noncanonical base pair (bp), designated as the $\eta'-\eta''$ interaction (Fig. 2a). After the branching reaction (2S and post-2S), D6 translocated to allow 3'-exon docking enabled by interactions with D1c ($\pi'-\pi$) and D2 ($\eta'-\eta$), as previously observed in canonical group II introns (Fig. 2b,c)^{8,9,26,34,35,37,38}.

Previous studies have reported that branchpoint A could undergo dynamics, either forming a one-nucleotide or two-nucleotide bulge^{39,40}. In the pre-1S state, the inactive A127 flips inside D6 and stacks with the 5'-SS G220 (Fig. 1d), forming a two-nucleotide bulge with local shifts of the surrounding nucleotides (Extended Data Fig. 6a). In the 1S state, we observed the one-nucleotide bulged A127 pointing outside of D6, with 2'-OH in close proximity of 2.8 Å to 5'-SS scissile phosphate ready for the branching reaction (Fig. 1e and Extended Data Fig. 6b), stabilized by stacking with G220 and forming a base triple with G101-C125, analogous to the bulged A recognition pattern recently reported in prebranching structures of both canonical group II introns and spliceosomes (Extended Data Fig. 6c,d)^{8,9,41,42}. In 2S and post-2S, A127 branched with G220 is translocated 20 Å away, facilitated by a 65° conformational change of D6, to allow docking of the 3'-exon in the catalytic core, ready for ligation (Figs. 1f,g and 2d).

Rearrangement of 5'-exon-IBS3 pairing for 3'-SS recognition

The *Cte1* intron sequence downstream of D6 presents 3'- and 5'-exons with intron-binding sites (IBS1 and IBS3) that recognize EBSs in D1 (refs. 43,44). Three exon-binding sites (EBS1–3) have been previously identified to complementarily base pair with IBS1–3 in exons (EBS–IBS) in different classes of canonical group II introns⁴³. The *Cte1* intron contains EBS1 and EBS3, which are analogous to group IIA introns¹. EBS1 is found in a terminal loop in D1d, which forms the 6-bp EBS1–IBS1, including an A543-A216 sheared pair in all structures except for post-2S (Extended Data Fig. 4a–d). In 1S, we observed additional density of 5'-exon base pairing with the IBS3 region of the 3'-exon (Fig. 2e and Extended Data Fig. 4b). In 2S, the 3'-exon undergoes a conformational change along with D6 to form an EBS3–IBS3 that includes a noncanonical base pair (C135-C538), which is analogous to the conventional group IIA intron δ–δ' interaction, to allow docking of the 3'-exon for ligation (Fig. 2d,f and Extended Data Fig. 4c)³⁵.

Unexpectedly, a three-nucleotide strand (C535-G537) upstream of EBS3 in the same EBS loop forms a major groove interaction, consisting of three base triples that reinforce EBS1–IBS1, which is

Table 1 | Cryo-EM data collection, processing and model refinement statistics of CP group II introns during back-splicing

Data collection and processing	Cte 1 pre-1S (EMD- 38649), (PDB 8XTS)	Cte 11S (EMD- 38647), (PDB 8XTQ)	Cte 12S (EMD- 38648), (PDB 8XTR)	Cte 1 post-2S (EMD- 38646), (PDB 8XTP)	Pla 2S (EMD- 60833), (PDB 9IS7)
Microscope	Titan Krios				
Voltage (kV)	300				
GIF quantum energy filter slit width (eV)	20				
Detector	Gatan K2 Summit				
Nominal magnification	×165,000				
Pixel size (Å)	0.85				
Symmetry imposed	C1				
Defocus range (μm)	-0.8 to -1.5				
Electron exposure (e ⁻ /Å ²)	59	59	59	64	58
Micrographs (acquired/used)	14,580/14,426	9,449/9,371	5,131/4,990	3,591/3,542	1,478/1,455
Number of extracted particles	11,716,479	7,295,013	4,421,466	2,688,017	811,161
Number of particles after 2D classification	4,435,066	2,274,274	2,160,792	871,757	277,273
Number of particles forwarded to 3D refinement	302,316	46,777	65,386	63,189	33,739
Map resolution (at 0.143 FSC criterion) (Å)	2.5	2.9	2.6	2.8	2.9
Local resolution range (Å)	2.2–6.2	2.6–8.5	2.4–10.2	2.4–8.3	2.4–8.3
Sharpening B factor (Å ²)	-76	-52	-59	-51	-45
Model refinement and validation					
Atoms	15,794	16,087	15,952	15,713	15,216
Residues	732	746	740	728	705
CC _{mask}	0.81	0.75	0.71	0.75	0.77
Resolution _{FSC} map versus model @ 0.5(Å)	2.7	3.0	3.1	3.0	3.0
Bond length (Å)	0.003	0.003	0.003	0.003	0.005
Bond angle (°)	0.651	0.587	0.712	0.587	0.878
Clashscore	2.6	2.1	2.4	2.1	3.5
Molprobity score	2.2	2.1	2.2	2.1	2.3

usually facilitated by IEP in canonical group II introns (Fig. 2g–j)^{8,9,26,35,38}. Following release of the circular exon product in post-2S, the EBS loop stabilizes through local rearrangement, forming two internal base triples, C535-G537-C545 and U536-G539-A543 (Fig. 2j).

Unexpected tertiary interactions with allosteric effects

Multiple interactions that have not been previously described in canonical group II introns were identified in the *Cte 1* intron. They were designated with new Greek letters, with lower-case letters representing interactions near the catalytic core and upper-case letters in the peripheral domains (Extended Data Fig. 7a and Supplementary Table 1). P1 and P2 were both predicted to form pseudoknot (PK) interactions on the basis of comparative genomics analysis, and the predicted P2–D2 PK was more conserved and could affect catalytic activity^{17,45}. Our *Cte 1* cryo-EM structures revealed that P1 forms a PK with the D2 terminal loop, whereas P2 forms another PK with a terminal loop at the 3' end of D3 (Γ'-Γ and Δ'-Δ) (Fig. 3a–c). The P2–D3 PK density was not well resolved in 1S and 2S when D6 and exons carried out large conformational changes (Fig. 1c), consistent with the prediction that PK interaction involving D2 is more stabilized¹⁷.

D1 (including D1a–D1d subdomains) forms numerous interactions with all domains of the intron to serve as the scaffold for correct folding, exon recognition and catalytic core organization. Previously unseen interactions have been observed in the peripheral regions, including three GAAA tetraloop/tetraloop receptor (TL/TLR) interactions between D1 and D1c (ξ-ξ') and D1b and D1c (A-A' and B-B'), a base triple between D1c and D2 (v-v') and a PK between D1d and D3 (o-o')

(Fig. 3d–h). Mutations that disrupted individual interactions in the peripheral regions significantly reduced catalytic activity compared to the wild-type (WT) sequence, suggesting that most of these interactions have allosteric effects on CP intron catalysis (Fig. 3i and Extended Data Fig. 7a). These effects are likely caused by the close proximities of ξ-ξ', A-A' and B-B' to D6 in pre-1S and 1S, v-v' and Γ'-Γ to D6 in 2S and post-2S, and o-o' to the catalytic triad (Figs. 2d and 3), resulting in stabilizations of the nearby regions of the catalytic triad and dynamic D6 that are essential to catalysis. Mutation of the P2–D3 PK interaction Δ'-Δ, far away from the catalytic triad and D6, did not affect catalysis of the *Cte 1* intron, consistent with the previous result that CP introns without this PK interaction remained catalytically active¹⁷.

Additional conserved interactions in group II introns include D1c and D2 (θ-θ') interaction, which secures the critical ε-ε' region in position for 5'-SS selection and catalysis^{8,46}, the peripheral interaction between D1b and D1d (α-α')⁴⁷ and interactions within D1d (ω-ω' and σ-σ') to reinforce positioning of the D5 catalytic core (Extended Data Fig. 7b–f)^{9,25}. D2 and D3, next to D1, are crucial for intron catalysis efficiency by forming the aforementioned interactions with D5 and D6 (refs. 34,48). Moreover, junction J2/3 directly interacts with the catalytic triad in D5 to form the catalytic triplex, which is reinforced by an interaction between D2 and D3 (p-p') (Extended Data Fig. 7g)^{34,49,50}. All interactions are summarized in Supplementary Table 1.

Metal ions enable folding and catalysis in the *Cte 1* intron

Metal ions are essential for ribozyme folding and catalysis^{51,52}. The catalytic core of the *Cte 1* intron is organized in D5 with J2/3 and a

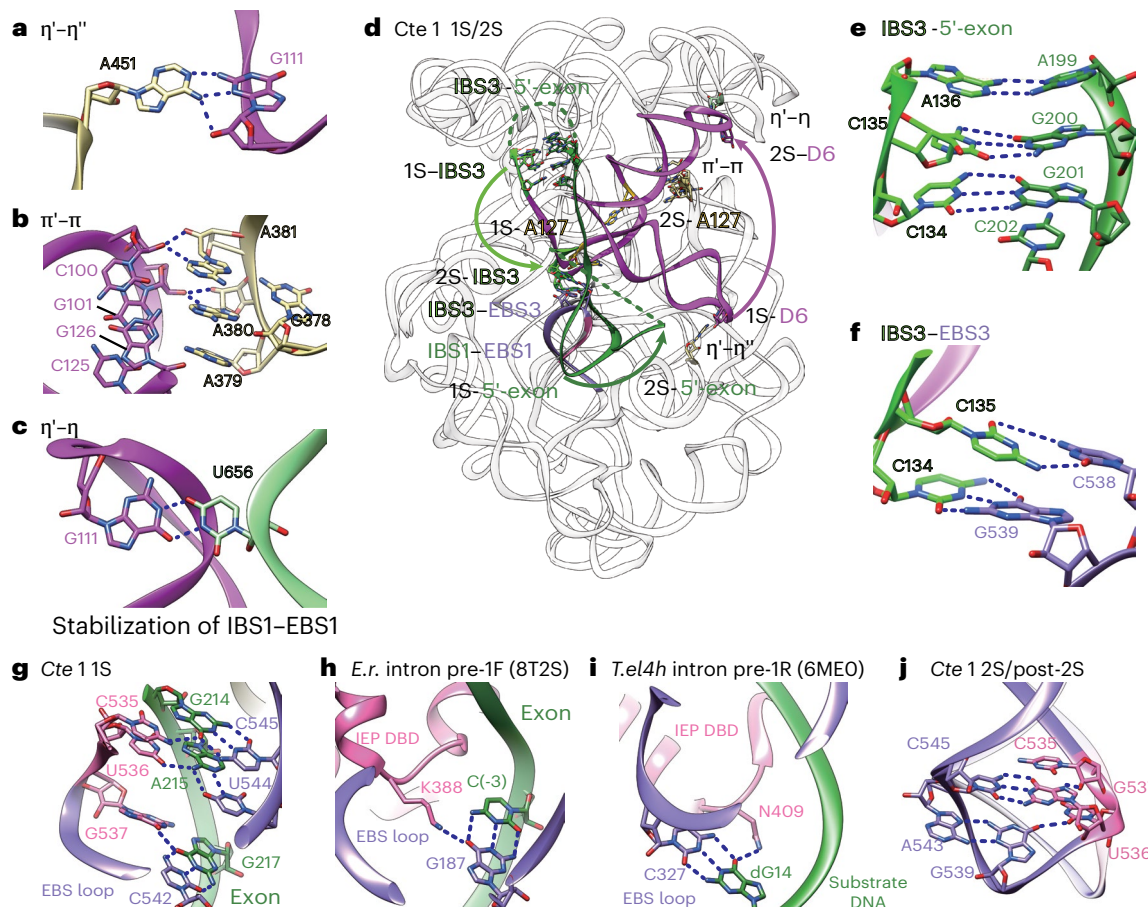


Fig. 2 | Conformational change of D6 facilitates rearrangement of 5'-exon-IBS3 base pairing for novel 3'-SS recognition. **a**, η' - η'' interaction, which stabilizes D6 in pre-1S and 1S. **b**, π' - π TL/TLR interaction, which stabilizes D6 in 2S and post-2S. **c**, η' - η interaction, which stabilizes D6 in 2S and post-2S. **d**, Conformational changes of D6, 5'-exon and 3'-exon between 1S and 2S. **e**, New 5'-exon-IBS3 base pairing in 1S. **f**, The 2-bp IBS3-EBS3 interaction in 2S. **g**, Major groove interaction

of EBS loop that reinforces the IBS1-EBS1 interaction. **h**, K388 from IEP stabilizes IBS-EBS in *E. r.* intron splicing. **i**, N409 from IEP stabilizes IBS-EBS in *T. el4h* intron splicing. **j**, EBS loop rearrangement in post-2S (purple), which forms new internal base triples compared to 2S (light purple). Blue dashed lines indicate hydrogen bonds, green dashed lines indicate unresolved exons, colored arrows indicate conformational changes from 1S to 2S.

two-nucleotide bulge that crucially binds to divalent metal ions M_1 and M_2 (refs. 53,54). In pre-1S, M_1 and M_2 coordinate with nonbridging oxygens of A60 and G61 in the catalytic triad, G83 in the two-nucleotide bulge and C81 adjacent to the λ' - λ interaction to establish the catalytic core. In the meantime, coordination of M_1 and M_2 with G220 pro- R_p , and of M_2 with the U219 bridging oxygen, stabilize the leaving group (Fig. 4a). Additionally, K_1 coordinates with A60, G61, G83 and G696 to further stabilize the catalytic triad, whereas K_2 coordinates with G224 in D1 and A695 of the γ - γ' interaction, which is critical for catalytic activity³⁶. A previously unreported metal ion, termed M_{35} , is clamped by nonbridging oxygens of A422 and U423 next to the λ - λ' interaction, and coordinates with U218 to hold the 5'-exon in place. This role of 5'-exon stabilization is normally played by the maturase DNA-binding domain in the canonical group II introns and Yju2 and Prp8 proteins in spliceosomes (Extended Data Fig. 4g-i)^{6,25,28}. Together these ions establish the conserved heteronuclear metal ion center that is present in all states of *Cte 1* intron catalysis (Fig. 4).

In the 1S state ready for branching, A127 flips toward the catalytic site and the 2'-OH nucleophile is coordinated with M_1 , whereas M_2 remains coordinating with U219 and G220 to prepare for the nucleophilic attack (Fig. 4b). After branching in 2S, the A127-G220 linkage moves away from the catalytic site to allow 3'-exon docking, in which the C134 leaving group is stabilized by M_1 , while the 5'-exon U219 3'-OH nucleophile is coordinated by M_2 to prepare for the second transesterification reaction (Fig. 4c). In post-2S after the

ligation, M_1 , M_2 and K_1 remain in position and K_2 shifts 4.3 Å to coordinate with C223 (Fig. 4d). The A695-U133 γ - γ' interaction is stacked by G221, G220 and A127, which brings the 3'-SS U133 closer to the catalytic core to coordinate with M_1 and M_{36} (Fig. 4d and Extended Data Fig. 4d). M_{36} is another unexpected metal ion that appears in the catalytic core to coordinate with U133 2'-OH. The interaction network of U133 in the catalytic core of post-2S is similar to 3'-SS in previous group II intron lariat forms ready for reverse splicing (Extended Data Fig. 4d-f)^{8,39}.

Previous studies have systematically evaluated 32 monovalent metal ion-binding sites (K^+) and 34 divalent metal ion-binding sites (M^{2+}) in group IIC intron crystal structures^{28,55}. A total of 60 metal ions were identified in each cryo-EM structure of different states in *Cte 1* intron splicing, including designation of 7 K^+ and 8 M^{2+} ions analogous to those previously identified in the group IIC intron⁵⁵. The rest of the metal ions are numbered M_{35} - M_{81} as K^+ and M^{2+} are indistinguishable in cryo-EM density under such resolution (Supplementary Table 2). Similar to other group II introns, the majority of metal ions reside in D1, suggesting that correct folding of D1 is critical to proceed with proper folding of the entire *Cte 1* intron (Extended Data Fig. 8a)^{56,57}. A metal core coordinated by M_{44} and M_{45} is similar to that previously described in the P4-P6 domain of the group I intron (Extended Data Fig. 8b)⁵⁸. A metal ion M_{64} resides in the major groove of the newly identified o-o' interaction (Fig. 3h). In addition, we observed M_5 , K_3 and K_4 close to the catalytic core but not directly interacting with

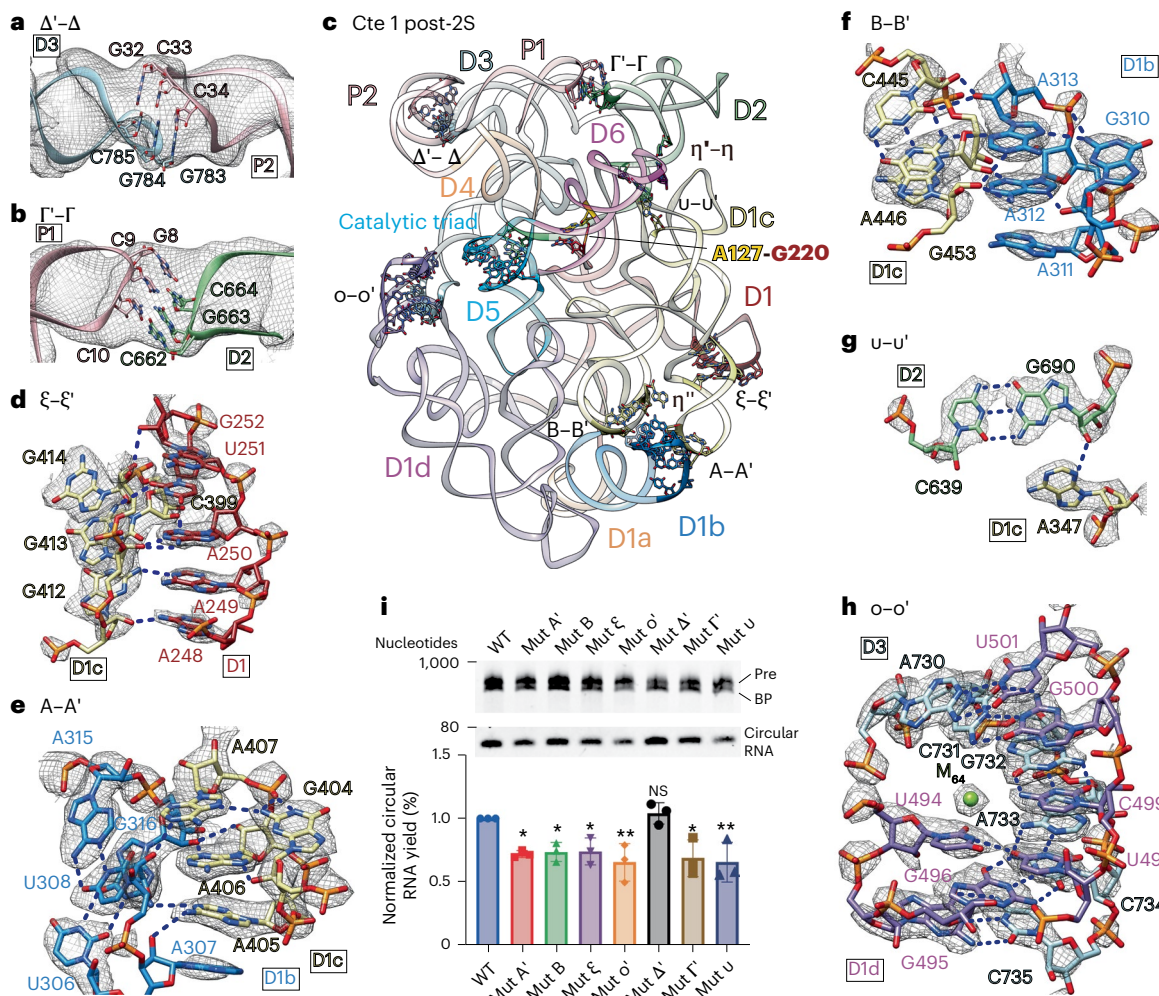


Fig. 3 | Cryo-EM density and models of novel tertiary interactions of Cte 1 intron. **a**, $\Delta'-\Delta$ PK between P2 and D3. **b**, $\Gamma'-\Gamma$ PK between P1 and D2. **c**, Overall architecture of Cte 1 intron in post-2S state with novel tertiary interactions highlighted. **d**, $\xi-\xi'$ minor groove interaction between D1 and D1c. **e**, A-A' TL/TLR between D1b and D1c. **f**, B-B' TL/TLR between D1b and D1c. **g**, $u-u'$ base triple consisting of A347-C639-G690 between D1c and D2. **h**, $o-o'$ PK interaction between D1d and D3 with a U494-U498-A733 base triple. **i**, Gel electrophoresis and quantification of circRNA product fractions of WT Cte 1 and corresponding

mutants (Mut) after carrying out the splicing reactions for 30 min. Data points in **i** represent each biological replicate. Colored bars and error bars are presented as mean values \pm standard deviation (s.d.) from three independent experiments. The exact *P* values are 0.029, 0.042, 0.046, 0.007, 0.995, 0.014 and 0.007 determined using a one-way analysis of variance (ANOVA). Statistical significance is denoted as **P* < 0.05, ***P* < 0.01; NS, no significant difference. Blue dashed lines indicate hydrogen bonds.

the reaction residues, which potentially have allosteric effects in catalysis by stabilizing the catalytic core, as previously described (Extended Data Fig. 8c)⁵⁵.

The unique features in the Cte 1 intron are common in CP introns

Although the Cte 1 intron back-splicing process shares common features with the canonical group II introns and spliceosomes, our cryo-EM structures have revealed several mechanistic insights unique to the CP group II intron. These include 5'- and 3'-exon interaction, 3'-SS recognition and M_{35} stabilization of the 5'-exon. To test whether these findings are common among other CP group II introns, we performed comparative genomics analysis based on the curated secondary structure derived from our cryo-EM structures (Extended Data Fig. 5a). This led to the discovery of more CP group II introns from new bacterial strains, in addition to those previously reported (Extended Data Fig. 9a)¹⁷. Sequences from *Acetobacter persici* (*Ape*), *Enterococcus faecalis* (*Efa*), *Gluconobacter* sp. Dm-44 (*Glu*), *Klebsiella pneumoniae* (*Kpn*), *Pla* and *Pollutimonas nitritireducens* (*Pni*) were evaluated for catalytic activity

and all were active except for the *Efa* intron (Extended Data Fig. 9b). The IVT product of the *Pla* intron was directly subjected to cryo-EM analysis, and we obtained the final reconstruction in the 2S state at a resolution of 2.9 Å (Extended Data Fig. 9c). The cryo-EM structure of the *Pla* intron revealed the 5'-exon-IBS3 base-pairing interaction, the 2-bp EBS3-IBS3 recognition and M_{35} stabilizing the 5'-exon (Extended Data Fig. 10), all of which were consistent with those features previously described in the Cte 1 intron, suggesting that these are unique to and conserved in CP group II introns.

Discussion

Naturally occurring circular permutations have been previously found in catalytic RNAs^{17,59–62}, rRNAs⁶³ and tRNAs⁶⁴. For self-cleaving catalytic RNAs, such as twister and hammerhead ribozymes that carry out cleavage of a single RNA strand within themselves, permutations have minimal effects on their functions and catalysis products as long as the catalytic core structure of permuted ribozymes remains intact^{59,65}. However, large self-splicing ribozymes, such as group I and group II introns, undergo both cleavage and ligation reactions, and the ligation

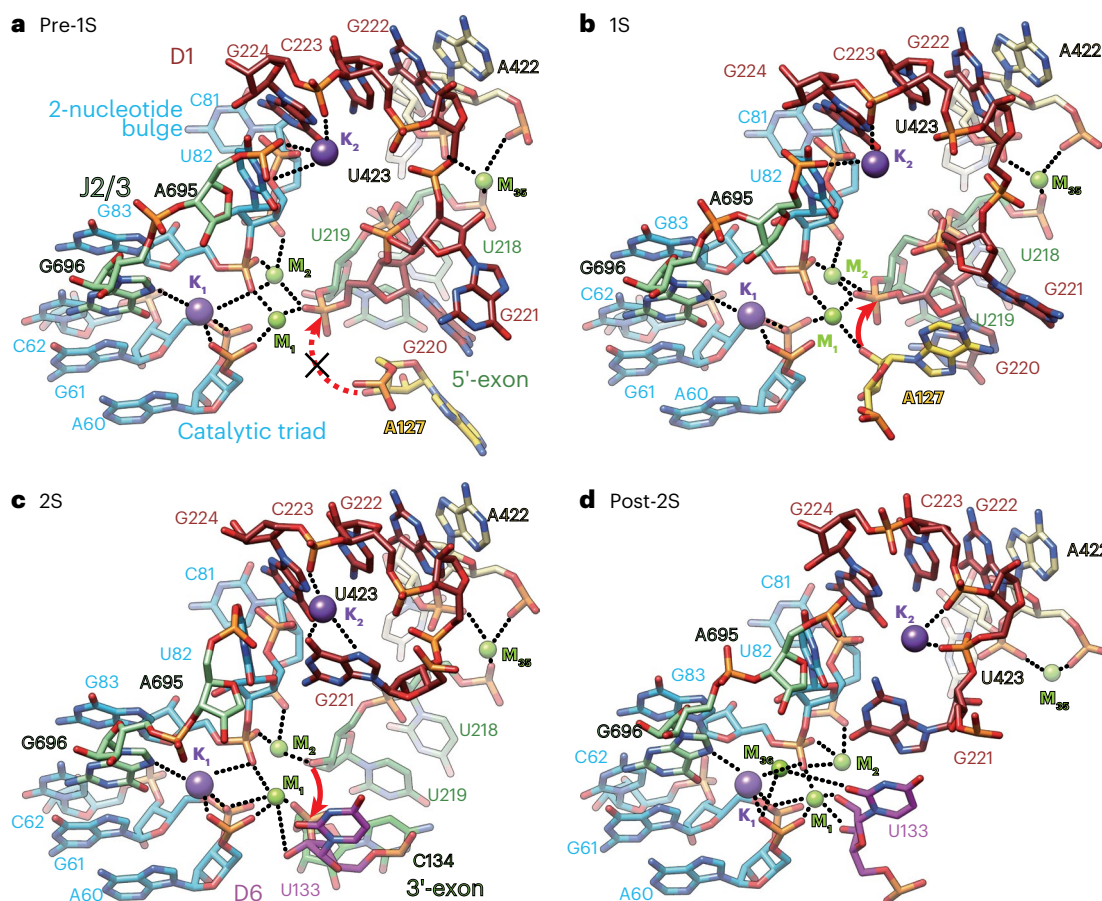


Fig. 4 | Metal ion composition in the catalytic core of different states reveal mechanism of *Cte 1* intron self-splicing. **a–d**, Metal ion coordination patterns in: pre-1S state before branching reaction (**a**), 1S state ready for branching (**b**), 2S

state ready for ligation reaction (**c**) and post-2S state after ligation with released circular exons (**d**). Black dashed lines indicate metal ion coordination, red arrows indicate nucleophilic attacks.

reactions of CP introns with swapped 5' and 3' domains lead to circular instead of linear exon products^{17,62}.

Circular RNAs have played emerging roles in regulation of gene expression, sequestration of proteins and microRNAs and modulation of signaling pathways and innate immune responses^{15,66,67}. They can also serve as translation templates if embedded with internal ribosome entry sites or m⁶A modifications^{68–71}. The abovementioned characteristics and superior stability of circRNAs have promoted numerous potential biomedical applications, including development of circRNA biomarkers⁷², circRNA interference of disease-related proteins and RNAs¹⁵ and circRNA vaccines supplementing the widely used mRNA vaccines¹⁶. However, efficient generation of circRNAs remains challenging¹⁵.

Although artificially designed CP introns were demonstrated to generate circRNA products decades ago^{13,14}, structural information of CP introns carrying out the back-splicing process remains unknown, which greatly limits our understanding of the circular exon generation mechanism. In this study we determine four cryo-EM structures associated with different states of *Cte 1* CP group II intron catalysis (Fig. 1) and elucidate mechanistic findings that are unique to CP intron back-splicing (Fig. 5 and Supplementary Video 1). Unlike canonical group II introns that retain only minimal catalytic activity without IEP, the *Cte 1* intron remains catalytically active by introducing the following unique structural features to compensate for the absence of protein: (1) η' – η' and η' – η tertiary interactions of the D6 T-loop that facilitate a 65° conformational change of D6 after branching reaction instead of IEP, which is analogous to canonical group II introns and spliceosomes (Fig. 2c–f); (2) the base-paired 5'-exon and 3'-exon both

undergo rearrangements along with D6 translocation to form the 2-bp EBS3–IBS3 while retaining the canonical EBS1–IBS1 ready for circular exon ligation (Fig. 2a–c); (3) EBS1 is stabilized by an unexpected major groove interaction whose role is normally played by maturase DNA-binding domain or thumb-X domains (Fig. 2g–j); (4) additional tertiary interactions in the peripheral domains stabilize the nearby regions of the catalytic triad and D6 T-loop in different conformations to make the catalytic core more compact for catalysis without IEP (Fig. 3, Extended Data Fig. 7 and Supplementary Table 1)¹⁷; and (5) an unforeseen metal ion, M₃₅, is found close to the heteronuclear metal center to stabilize the 5'-exon, a role that is normally played by proteins in canonical group II introns or spliceosomes (Fig. 4 and Extended Data Fig. 4).

Further comparative genomics analysis identifies more CP group II introns in other bacteria that are catalytically active in the absence of IEP. Cryo-EM study of the *Pla* CP intron demonstrates that all these unique structural features are conserved among CP group II introns (Extended Data Figs. 9 and 10). Such conservation does not seem to support that CP group II introns arose incidentally¹⁷, so is it possible that they may be ancestral and canonical group II introns have evolved through a process such as constructive neutral evolution⁷³? After all, complexed RNA structural features in molecular machines are usually seen as relics of the RNA world and more proteins and less complexed RNAs often evolved to carry out the same functions during evolution, as demonstrated by RNase P, and group II introns, retrotransposons and spliceosomes^{6,74,75}. On the other hand, the evolutionary pathways of circular permutations mostly involve insertion of duplicated sequences (duplication mechanism) or swapping of partial domains (fission and

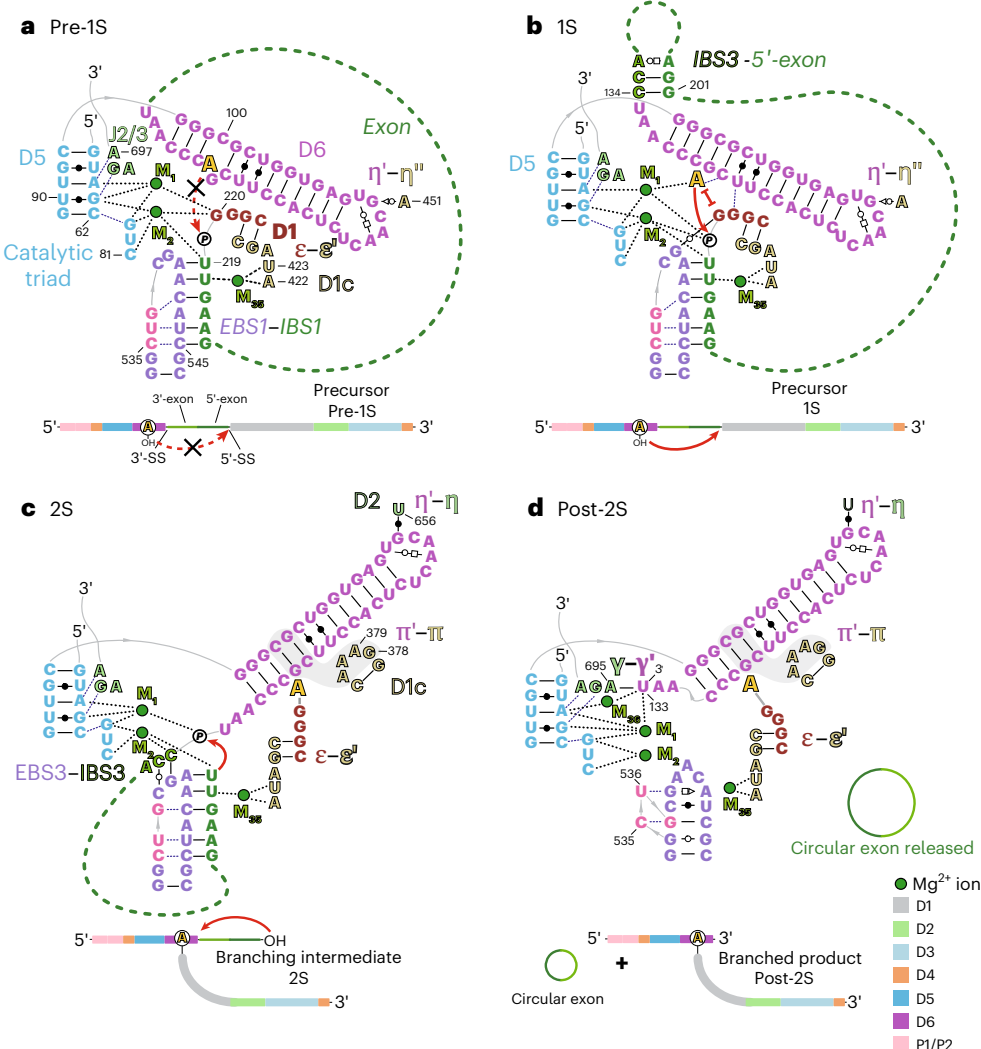


Fig. 5 | Schematic illustration of Cre1 intron self-splicing dynamics. **a**, In pre-1S, bulged A resides inside D6 and stays away from the 5'-SS, which cannot carry out the branching reaction, while the EBS1-IBS1 is stabilized by three base triples formed by the EBS loop. **b**, In 1S, bulged A flips out of D6 and forms a base triple with G101-C125 ready for the branching reaction, while 5'-exon forms a base-pairing interaction with IBS3. **c**, In 2S after branching, D6 undergoes conformational change with A127-G220 linkage, whereas the IBS3 rearranges

to form EBS3-IBS3 ready for circular exon ligation. **d**, In post-2S, the EBS loop rearranges to form two internal base triples after the circular exon is released. Green dashed lines indicate unresolved exons, black dashed lines indicate metal ion coordination, blue dotted lines indicate tertiary interactions forming base triples, gray solid lines with arrows indicate sequence direction from 5' to 3' end, red arrows indicate nucleophilic attack direction of the first and second step of splicing.

fusion mechanism), as demonstrated in proteins¹². However, all CP group II introns discovered so far do not encode maturase, and the resulting back-spliced intron product remains on the transcript¹⁷, making retrotransposition, like canonical group II introns, almost impossible. A more plausible pathway is probably that CP group II introns evolved from two or more juxtaposed canonical group II introns resulting from multiple retrotranspositions.

In conclusion, these results reveal the overall architecture of a novel CP group II intron and conformational changes and dynamics involved in the back-splicing process, which elucidate the mechanism of circular exon generation via two consecutive transesterification reactions, and potentially serve as the foundation for future applications in circRNA research and therapeutics, such as the design of novel CP introns with optimal efficiency to generate circRNAs of desired sequences.

Online content

Any methods, additional references, Nature Portfolio reporting summaries, source data, extended data, supplementary information,

acknowledgements, peer review information; details of author contributions and competing interests; and statements of data and code availability are available at <https://doi.org/10.1038/s41594-025-01484-x>.

References

- Pyle, A. M. Group II intron self-splicing. *Annu. Rev. Biophys.* **45**, 183–205 (2016).
- Lambowitz, A. M. & Zimmerly, S. Group II introns: mobile ribozymes that invade DNA. *Cold Spring Harb. Perspect. Biol.* **3**, a003616 (2011).
- Pyle, A. & Lambowitz, A. in *The RNA World* 3rd edn (eds Gesteland, R. F. et al.) 469–505 (Cold Spring Harbor Laboratory, 2006).
- Zimmerly, S. & Semper, C. Evolution of group II introns. *Mob. DNA* **6**, 7 (2015).
- Lambowitz, A. M. & Belfort, M. in *Mobile DNA III* (eds Chandler, M. et al.) 1209–1236 (ASM, 2015).
- Galej, W. P., Toor, N., Newman, A. J. & Nagai, K. Molecular mechanism and evolution of nuclear pre-mRNA and group II intron splicing: insights from cryo-electron microscopy structures. *Chem. Rev.* **118**, 4156–4176 (2018).

7. Wilkinson, M. E., Charenton, C. & Nagai, K. RNA splicing by the spliceosome. *Annu. Rev. Biochem.* **89**, 359–388 (2020).
8. Xu, L., Liu, T., Chung, K. & Pyle, A. M. Structural insights into intron catalysis and dynamics during splicing. *Nature* **624**, 682–688 (2023).
9. Haack, D. B. et al. Cryo-EM structures of a group II intron reverse splicing into DNA. *Cell* **178**, 612–623.e12 (2019).
10. Pan, T. & Uhlenbeck, O. C. Circularly permuted DNA, RNA and proteins—a review. *Gene* **125**, 111–114 (1993).
11. Grishin, N. V. Fold change in evolution of protein structures. *J. Struct. Biol.* **134**, 167–185 (2001).
12. Bliven, S. & Prlić, A. Circular permutation in proteins. *PLoS Comput. Biol.* **8**, e1002445 (2012).
13. Ford, E. & Ares, M. Synthesis of circular RNA in bacteria and yeast using RNA cyclase ribozymes derived from a group I intron of phage T4. *Proc. Natl Acad. Sci. USA* **91**, 3117–3121 (1994).
14. Jarrell, K. A. Inverse splicing of a group II intron. *Proc. Natl Acad. Sci. USA* **90**, 8624–8627 (1993).
15. Liu, C.-X. & Chen, L.-L. Circular RNAs: characterization, cellular roles, and applications. *Cell* **185**, 2016–2034 (2022).
16. Qu, L. et al. Circular RNA vaccines against SARS-CoV-2 and emerging variants. *Cell* **185**, 1728–1744.e16 (2022).
17. Roth, A., Weinberg, Z., Vanderschuren, K., Murdock, M. H. & Breaker, R. R. Natural circularly permuted group II introns in bacteria produce RNA circles. *iScience* **24**, 103431 (2021).
18. Chen, C. et al. A flexible, efficient, and scalable platform to produce circular RNAs as new therapeutics. Preprint at *bioRxiv* <https://doi.org/10.1101/2022.05.31.494115> (2022).
19. Ma, H., Jia, X., Zhang, K. & Su, Z. Cryo-EM advances in RNA structure determination. *Signal Transduct. Target. Ther.* **7**, 58 (2022).
20. Luo, B. et al. Cryo-EM reveals dynamics of *Tetrahymena* group I intron self-splicing. *Nat. Catal.* **6**, 298–309 (2023).
21. Li, S., Palo, M. Z., Zhang, X., Pintilie, G. & Zhang, K. Snapshots of the second-step self-splicing of *Tetrahymena* ribozyme revealed by cryo-EM. *Nat. Commun.* **14**, 1294 (2023).
22. Zhang, X., Li, S., Pintilie, G., Palo, M. Z. & Zhang, K. Snapshots of the first-step self-splicing of *Tetrahymena* ribozyme revealed by cryo-EM. *Nucleic Acids Res.* **51**, 1317–1325 (2023).
23. Steitz, T. A. & Steitz, J. A. A general two-metal-ion mechanism for catalytic RNA. *Proc. Natl Acad. Sci. USA* **90**, 6498–6502 (1993).
24. Heilman-Miller, S. L. & Woodson, S. A. Effect of transcription on folding of the *Tetrahymena* ribozyme. *RNA* **9**, 722–733 (2003).
25. Toor, N., Keating, K. S., Taylor, S. D. & Pyle, A. M. Crystal structure of a self-spliced group II intron. *Science* **320**, 77–82 (2008).
26. Haack, D. B., Rudolfs, B., Zhang, C., Lyumkis, D. & Toor, N. Structural basis of branching during RNA splicing. *Nat. Struct. Mol. Biol.* **31**, 179–189 (2024).
27. Erat, M. C. & Sigel, R. K. O. Divalent metal ions tune the self-splicing reaction of the yeast mitochondrial group II intron Sc.ai5y. *J. Biol. Inorg. Chem.* **13**, 1025–1036 (2008).
28. Marcia, M. & Pyle, A. M. Visualizing group II intron catalysis through the stages of splicing. *Cell* **151**, 497–507 (2012).
29. Nguyen, T. H. D. et al. CryoEM structures of two spliceosomal complexes: starter and dessert at the spliceosome feast. *Curr. Opin. Struct. Biol.* **36**, 48–57 (2016).
30. Boudvillain, M., de Lencastre, A. & Pyle, A. M. A tertiary interaction that links active-site domains to the 5' splice site of a group II intron. *Nature* **406**, 315–318 (2000).
31. Costa, M. & Michel, F. Frequent use of the same tertiary motif by self-folding RNAs. *EMBO J.* **14**, 1276–1285 (1995).
32. Boudvillain, M. & Marie Pyle, A. Defining functional groups, core structural features and inter-domain tertiary contacts essential for group II intron self-splicing: a NAIM analysis. *EMBO J.* **17**, 7091–7104 (1998).
33. Fedorova, O. & Pyle, A. M. Linking the group II intron catalytic domains: tertiary contacts and structural features of domain 3. *EMBO J.* **24**, 3906–3916 (2005).
34. Robart, A. R., Chan, R. T., Peters, J. K., Rajashankar, K. R. & Toor, N. Crystal structure of a eukaryotic group II intron lariat. *Nature* **514**, 193–197 (2014).
35. Qu, G. et al. Structure of a group II intron in complex with its reverse transcriptase. *Nat. Struct. Mol. Biol.* **23**, 549–557 (2016).
36. Jacquier, A. & Michel, F. Base-pairing interactions involving the 5' and 3'-terminal nucleotides of group II self-splicing introns. *J. Mol. Biol.* **213**, 437–447 (1990).
37. Liu, N. et al. Exon and protein positioning in a pre-catalytic group II intron RNP primed for splicing. *Nucleic Acids Res.* **48**, 11185–11198 (2020).
38. Chung, K. et al. Structures of a mobile intron retroelement poised to attack its structured DNA target. *Science* **378**, 627–634 (2022).
39. Costa, M., Walbott, H., Monachello, D., Westhof, E. & Michel, F. Crystal structures of a group II intron lariat primed for reverse splicing. *Science* **354**, aaf9258 (2016).
40. Planger, R. et al. Branch site bulge conformations in domain 6 determine functional sugar puckers in group II intron splicing. *Nucleic Acids Res.* **47**, 11430–11440 (2019).
41. Bertram, K. et al. Structural insights into the roles of metazoan-specific splicing factors in the human step 1 spliceosome. *Mol. Cell* **80**, 127–139.e6 (2020).
42. Wilkinson, M. E., Fica, S. M., Galej, W. P. & Nagai, K. Structural basis for conformational equilibrium of the catalytic spliceosome. *Mol. Cell* **81**, 1439–1452.e39 (2021).
43. Jacquier, A. & Michel, F. Multiple exon-binding sites in class II self-splicing introns. *Cell* **50**, 17–29 (1987).
44. Costa, M., Michel, F. & Westhof, E. A three-dimensional perspective on exon binding by a group II self-splicing intron. *EMBO J.* **19**, 5007–5018 (2000).
45. Weinberg, Z. et al. Detection of 224 candidate structured RNAs by comparative analysis of specific subsets of intergenic regions. *Nucleic Acids Res.* **45**, 10811–10823 (2017).
46. Costa, M., Dème, E., Jacquier, A. & Michel, F. Multiple tertiary interactions involving domain II of group II self-splicing introns. *J. Mol. Biol.* **267**, 520–536 (1997).
47. Harris-Kerr, C. L., Zhang, M. & Peebles, C. L. The phylogenetically predicted base-pairing interaction between alpha and alpha' is required for group II splicing in vitro. *Proc. Natl Acad. Sci. USA* **90**, 10658–10662 (1993).
48. Fedorova, O., Mitros, T. & Pyle, A. M. Domains 2 and 3 interact to form critical elements of the group II intron active site. *J. Mol. Biol.* **330**, 197–209 (2003).
49. Mikheeva, S., Murray, H. L., Zhou, H., Turczyk, B. M. & Jarrell, K. A. Deletion of a conserved dinucleotide inhibits the second step of group II intron splicing. *RNA* **6**, 1509–1515 (2000).
50. de Lencastre, A. & Pyle, A. M. Three essential and conserved regions of the group II intron are proximal to the 5'-splice site. *RNA* **14**, 11–24 (2008).
51. Lambert, D., Leipply, D., Shiman, R. & Draper, D. E. The influence of monovalent cation size on the stability of RNA tertiary structures. *J. Mol. Biol.* **390**, 791–804 (2009).
52. Woodson, S. A. Metal ions and RNA folding: a highly charged topic with a dynamic future. *Curr. Opin. Chem. Biol.* **9**, 104–109 (2005).
53. Gordon, P. M. & Piccirilli, J. A. Metal ion coordination by the AGC triad in domain 5 contributes to group II intron catalysis. *Nat. Struct. Biol.* **8**, 893–898 (2001).
54. Sontheimer, E. J., Gordon, P. M. & Piccirilli, J. A. Metal ion catalysis during group II intron self-splicing: parallels with the spliceosome. *Genes Dev.* **13**, 1729–1741 (1999).

55. Marcia, M. & Pyle, A. M. Principles of ion recognition in RNA: insights from the group II intron structures. *RNA* **20**, 516–527 (2014).
56. Su, L. J., Waldsich, C. & Pyle, A. M. An obligate intermediate along the slow folding pathway of a group II intron ribozyme. *Nucleic Acids Res.* **33**, 6674–6687 (2005).
57. Pyle, A. M., Fedorova, O. & Waldsich, C. Folding of group II introns: a model system for large, multidomain RNAs? *Trends Biochem. Sci.* **32**, 138–145 (2007).
58. Cate, J. H. et al. Crystal structure of a group I ribozyme domain: principles of RNA packing. *Science* **273**, 1678–1685 (1996).
59. Roth, A. et al. A widespread self-cleaving ribozyme class is revealed by bioinformatics. *Nat. Chem. Biol.* **10**, 56–60 (2014).
60. Weinberg, C. E., Weinberg, Z. & Hammann, C. Novel ribozymes: discovery, catalytic mechanisms, and the quest to understand biological function. *Nucleic Acids Res.* **47**, 9480–9494 (2019).
61. Jimenez, R. M., Polanco, J. A. & Lupták, A. Chemistry and biology of self-cleaving ribozymes. *Trends Biochem. Sci.* **40**, 648–661 (2015).
62. Chi, S. I., Dahl, M., Emblem, Å. & Johansen, S. D. Giant group I intron in a mitochondrial genome is removed by RNA back-splicing. *BMC Mol. Biol.* **20**, 16 (2019).
63. Birkedal, U., Beckert, B., Wilson, D. N. & Nielsen, H. The 23S ribosomal RNA from *Pyrococcus furiosus* is circularly permuted. *Front. Microbiol.* **11**, 582022 (2020).
64. Soma, A. Circularly permuted tRNA genes: their expression and implications for their physiological relevance and development. *Front. Genet.* **5**, 63 (2014).
65. Hammann, C., Lupták, A., Perreault, J. & de la Peña, M. The ubiquitous hammerhead ribozyme. *RNA* **18**, 871–885 (2012).
66. Chen, L.-L. The expanding regulatory mechanisms and cellular functions of circular RNAs. *Nat. Rev. Mol. Cell Biol.* **21**, 475–490 (2020).
67. Xiao, M.-S., Ai, Y. & Wilusz, J. E. Biogenesis and functions of circular RNAs come into focus. *Trends Cell Biol.* **30**, 226–240 (2020).
68. Chen, C.-Y. & Sarnow, P. Initiation of protein synthesis by the eukaryotic translational apparatus on circular RNAs. *Science* **268**, 415–417 (1995).
69. Pamudurti, N. R. et al. Translation of CircRNAs. *Mol. Cell* **66**, 9–21.e7 (2017).
70. Chen, C.-K. et al. Structured elements drive extensive circular RNA translation. *Mol. Cell* **81**, 4300–4318.e13 (2021).
71. Yang, Y. et al. Extensive translation of circular RNAs driven by N6-methyladenosine. *Cell Res.* **27**, 626–641 (2017).
72. Litke, J. L. & Jaffrey, S. R. Highly efficient expression of circular RNA aptamers in cells using autocatalytic transcripts. *Nat. Biotechnol.* **37**, 667–675 (2019).
73. Gray, M. W., Lukeš, J., Archibald, J. M., Keeling, P. J. & Doolittle, W. F. Irremediable complexity? *Science* **330**, 920–921 (2010).
74. Zhou, B. et al. Coevolution of RNA and protein subunits in RNase P and RNase MRP, two RNA processing enzymes. *J. Biol. Chem.* **300**, 105729 (2024).
75. Deng, P. et al. Structural RNA components supervise the sequential DNA cleavage in R2 retrotransposon. *Cell* **186**, 2865–2879.e20 (2023).

Publisher's note Springer Nature remains neutral with regard to jurisdictional claims in published maps and institutional affiliations.

Springer Nature or its licensor (e.g. a society or other partner) holds exclusive rights to this article under a publishing agreement with the author(s) or other rightsholder(s); author self-archiving of the accepted manuscript version of this article is solely governed by the terms of such publishing agreement and applicable law.

© The Author(s), under exclusive licence to Springer Nature America, Inc. 2025

Methods

Cte 1 intron splicing following in vitro transcription

RNAs were prepared following the recently reported protocol⁷⁶. In brief, the full-length *C. testosteroni* KF-1 (*Cte 1*) group II intron sequence was derived from NCBI (GenBank: NZ_AAUJ02000001.1). DNA templates in pUC-19 plasmid were amplified using the primers listed in Supplementary Table 3, in which 'Me' refers to methoxyl modification, which was introduced to ensure sequence homogeneity at the 3' end of the amplified DNA template and subsequent RNA product⁷⁷. The resulting DNA templates were isolated by ethanol precipitation for subsequent IVT reactions. Splicing reactions were carried out by IVT containing 0.3 μM DNA templates, 10 mM NTP mixture, 40 mM Tris–HCl (pH 7.9), 20 mM MgCl₂, 2 mM spermidine, 0.01% TritonX-100, 10 mM DTT, 1 U μl⁻¹ RNase inhibitor (Thermo Scientific), 0.1 U μl⁻¹ pyrophosphatase (Thermo Scientific) and 7.5 U μl⁻¹ T7 RNA polymerase (prepared in-house) and incubated at 37 °C for 30 min (ref. 20). The IVT product was mixed with 2× denaturing gel loading buffer containing 95% formamide, 0.025% SDS, 10 mM EDTA, 0.025% xylene cyanol and 0.025% bromophenol blue, and loaded on a 6% 29:1 acrylamide:bis, 7 M urea polyacrylamide gel. The gel was run at 25 W for 2 h and stained for 5 min in SYBR Gold (Invitrogen) and visualized using an ultraviolet (UV) transillumination molecular imager (Bio-Rad ChmiDoc XRS+).

RNA preparation of different *Cte 1* constructs

Mutated *Cte 1* constructs were prepared by PCR site-directed mutagenesis using the primers listed in Supplementary Table 3. To inhibit the self-splicing during IVT and purify the full-length precursor *Cte 1* intron, the IVT condition was modified as follows: 0.3 μM DNA templates, 40 mM NTP mixture, 40 mM Tris–HCl (pH 7.9), 100 mM MgCl₂, 2 mM spermidine, 0.01% TritonX-100, 10 mM DTT, 1 U μl⁻¹ RNase inhibitor, 0.1 U μl⁻¹ pyrophosphatase and 7.5 U μl⁻¹ T7 RNA polymerase and incubated at 37 °C for 2 h (ref. 78). After DNase I digestion followed by proteinase K treatment to discard DNA templates and proteins, the RNA product was mixed with 2× denaturing gel loading buffer and loaded on a 6% 29:1 acrylamide:bis, 7 M urea polyacrylamide gel. The gel was run at 25 W for 4 h, then visualized briefly with a 254-nm UV lamp. RNA was excised from the gel and eluted overnight in RNase-free water with 500 mM NaOAc and 20 mM EDTA at 4 °C, then purified by ethanol precipitation. The RNA sample quality was examined by electrophoresis on a denaturing 6% urea–PAGE gel and stored at –80 °C until further use.

CP group II intron in vitro self-splicing assay

Purified pre-RNA at a final concentration of 1 μM was heated to 80 °C for 1 min in 10 mM Tris–HCl pH 7.5 and 100 mM KCl, then slowly cooled to 60 °C and incubated at 37 °C for the designated time in the presence of 20 mM CaCl₂. Reactions were terminated with 2× denaturing gel loading buffer containing 95% formamide, 0.025% SDS, 10 mM EDTA, 0.025% xylene cyanol and 0.025% bromophenol blue. Products were loaded on a 6% 29:1 acrylamide:bis, 7 M urea polyacrylamide gel. The gel was run at 25 W for 2 h and stained for 5 min in SYBR Gold (Invitrogen) and visualized using a UV transillumination molecular imager (Bio-Rad ChmiDoc XRS+).

For other CP group II intron splicing activity and quantification of splicing efficiency of *Cte 1* mutants compared to WT *Cte 1*, splicing reactions were carried out in the abovementioned conditions and incubated at 37 °C for 30 min in the presence of 20 mM MgCl₂ instead of CaCl₂. Band intensities of pre-RNA, BP and circRNA were quantified by Bio-Rad Image Lab software. The circRNA product fraction was calculated using the following equation, in which / indicates gel band intensity and E indicates circRNA product fraction, and pre-RNA, BP and circRNA represent different bands, as shown in Fig. 3*i*. An ordinary ANOVA was performed using GraphPad Prism v.10.0, with a significance level set at *P* = 0.05:

$$E = \frac{(I_{BP} + I_{circRNA}) / I_{pre}}{(I_{BP-WT} + I_{circRNA-WT}) / I_{pre-WT}}$$

RNA sample preparation for cryo-EM

For the IVT reaction mixture, 200 μl was buffer exchanged with 1× transcription buffer using concentrator columns with a 50-kDa cutoff (Ultrafiltration Centrifugal Tube, Millipore) and concentrated to a final volume of 20 μl.

For splicing reaction products in the presence of CaCl₂, 200 μl reaction products at 5 min and 4 h time points were concentrated to 20 μl using prechilled concentrator columns with 50-kDa cutoff (Ultrafiltration Centrifugal Tube, Millipore). RNA concentration was quantified using a Nanodrop spectrophotometer (Thermo Scientific) and RNA quality was checked on a 6% 29:1 acrylamide:bis, 7 M urea polyacrylamide gel.

Cryo-EM sample preparation

A total of 3 μl of the abovementioned RNA samples (10 μM) were applied onto glow-discharged (10 s) 200-mesh R1.2-1.3 Quantifoil Cu grids with 2-nm continuous carbon film. After holding for 30 s, the grids were blotted for 1.5 s in 100% humidity at 4 °C with no blotting offset and rapidly frozen in liquid ethane using a Vitrobot Mark IV (Thermo Fisher).

Cryo-EM single-particle data acquisition and data processing

Four datasets were collected using the same cryo-EM microscope settings. Frozen grids were loaded into a Titan Krios (Thermo Fisher) operated at 300 kV, condenser lens aperture 50 μm, spot size 6, parallel beam with illuminated area of 1.03 μm in diameter. Microscope magnification was at ×165,000 (corresponding to a calibrated sampling of 0.85 Å per pixel).

For *Cte 1* pre-RNA splicing product for 5 min, 9,449 movie stacks were collected automatically using EPU software on a K2 direct electron camera equipped with a Bioquantum energy filter with an energy slit of 20 eV (Gatan), operating in counting mode at a recording rate of 5 raw frames per second and a total exposure time of 6 s, yielding 30 frames per stack, and a total dose of 59 e⁻/Å². All movie stacks were collected with defocus values ranging between –0.8 and –1.5 μm. These movie stacks were motion corrected using patch motion correction. After CTF correction by Patch CTF estimation, 9,371 micrographs were subjected to the Blob picker for automatic particle picking. A total of 8,916,089 particles were extracted with a box size of 320 × 320 pixels and were subjected to two rounds of two-dimensional (2D) classification in cryoSPARC v.4.4.1 (ref. 79). Representative 2D templates were selected for template-based particle picking by Template picker. After 2D classification, 2,274,274 particles were selected for ab initio reconstruction and heterogeneous refinement to reconstruct an initial model and discard bad particles. All remaining particles generated one reconstruction as a template for further classification. Three rounds of 3D classification resulted in 143,057 particles and 46,777 particles corresponding to the pre-1S and 1S states. Nonuniform refinement, CTF refinement, reference-based motion correction (RBMC) and nonuniform refinement of 1S yielded a final reconstruction at 2.9-Å resolution.

For *Cte 1* pre-RNA splicing product for 4 h, 5,131 movie stacks were collected and processed as mentioned above. Three rounds of 3D classification resulted in 161,408 particles and 65,386 particles corresponding to the pre-1S and 2S states. Homogeneous refinement and CTF refinement of 2S yielded a final reconstruction at 2.6-Å resolution, whereas particles of pre-1S from two datasets were combined to 302,316 particles for homogeneous refinement and CTF refinement that yielded a final reconstruction at 2.5-Å resolution.

For *Cte 1* IVT product, 3,591 movie stacks were collected and processed as mentioned above. After 2D classification, 871,757 particles were subjected to ab initio reconstruction and heterogeneous refinement to reconstruct an initial model containing 271,726 particles. After one round of 3D classification, 63,189 particles were selected for nonuniform (NU) refinement, CTF refinement and RBMC.

The final NU refinement yielded a final reconstruction of *Cte1* post-2S at 2.8-Å resolution.

For *Pla* IVT product, 1,478 movie stacks were collected and processed as mentioned above. Particles were automatically selected by the Blob picker. After 2D classification, 277,273 unbinned particles were subjected to ab initio reconstruction and heterogeneous refinement to reconstruct an initial model and discard bad particles. After homogeneous refinement and one round of 3D classification, a total of 108,902 particles corresponding to the *Pla* 2S states were subjected to NU refinement, CTF refinement and RBMC. The final NU refinement yielded a final reconstruction of *Pla* 2S at 2.9-Å resolution.

All global resolutions were estimated using the 0.143 criterion of the Fourier shell correlation (FSC) curve. Local resolution maps were determined, and low-pass filtered accordingly. All final maps were displayed in UCSF ChimeraX v.1.6 using local resolution low-pass filtered maps unless noted otherwise⁸⁰.

Cryo-EM model building and refinement

The *Cte1* and *Pla* models were built de novo with the assistance of auto-DRRAFTER and CryoREAD v.8.2 (refs. 81,82), then manually adjusted in Coot v.0.9.8 as needed⁸³. These models were refined with Phenix.real_space_refine in Phenix v.1.15 (ref. 84), yielding an averaged model-map correlation coefficient (CCmask) of 0.81, 0.75, 0.71, 0.75 and 0.77, respectively. Final models were validated with MolProbity v.4.5.1 and Q-score analysis^{85,86}.

Comparative genomics analysis

We used INFERNAL v.1.1.4 to construct a covariance model (CM) from the sequence and secondary structure of *Cte1* using cmbuild⁸⁷. This model was applied to search homologous sequences in the NCBI nucleotide dataset (<https://ftp.ncbi.nlm.nih.gov/blast/db/FASTA/nt.gz>) with cmsearch. The retrieved sequences were aligned to the CM using cmalign, incorporating both sequence and structural conservation. Finally, R-scape was used to evaluate and optimize the covariance-based secondary structure with parameters -s--cacofold--r2ral⁸⁸.

Figure preparation

Figures, illustrations and videos were prepared using Chimera v.1.16 (ref. 89), ChimeraX v.1.6, GraphPad Prism v.10.0, Adobe Illustrator 2020 and Adobe Premiere Pro 2020.

Reporting summary

Further information on research design is available in the Nature Portfolio Reporting Summary linked to this article.

Data availability

The cryo-EM maps and associated atomic coordinate models of *Comamonas testosteroni* KF-1 CP group II intron pre-1S, 1S, 2S and post-2S, and *Paracandidimonas lactea* strain Q2-2 CP group II intron 2S have been deposited in the wwPDB OneDep System under EMD accession codes EMD-38649, EMD-38647, EMD-38648, EMD-38646 and EMD-60833 and PDB codes 8XTS, 8XTQ, 8XTR, 8XTP and 9IS7, respectively. The NCBI nucleotide dataset (<https://ftp.ncbi.nlm.nih.gov/blast/db/FASTA/nt.gz>) was used for comparative analysis. Full-length WT and mutated *Comamonas testosteroni* KF-1 sequences were used according to NCBI (GenBank: NZ_AAUJ02000001.1). Full-length WT *Paracandidimonas lactea* strain Q2-2 sequence was used according to NCBI (GenBank: NZ_JAJJOZ000000000.1). Raw data for sequence and structure conservation analyses are included in Supplementary Data 1. All other data are available from the authors on reasonable request. Source data are provided with this paper.

References

76. Chen, X. et al. RNA sample optimization for cryo-EM analysis. *Nat. Protoc.* <https://doi.org/10.1038/s41596-024-01072-1> (2024).
77. Kao, C., Zheng, M. & Rüdisser, S. A simple and efficient method to reduce nontemplated nucleotide addition at the 3 terminus of RNAs transcribed by T7 RNA polymerase. *RNA* **5**, 1268–1272 (1999).
78. Inoue, T., Sullivan, F. X. & Cech, T. R. New reactions of the ribosomal RNA precursor of *Tetrahymena* and the mechanism of self-splicing. *J. Mol. Biol.* **189**, 143–165 (1986).
79. Punjani, A. et al. cryoSPARC: algorithms for rapid unsupervised cryo-EM structure determination. *Nat. Methods* **14**, 290–296 (2017).
80. Meng, E. C. et al. UCSF ChimeraX: tools for structure building and analysis. *Protein Sci.* **32**, e4792 (2023).
81. Ma, H. et al. Auto-DRRAFTER: automated RNA modeling based on cryo-EM density. *Methods Mol. Biol.* **2568**, 193–211 (2023).
82. Wang, X. et al. CryoREAD: de novo structure modeling for nucleic acids in cryo-EM maps using deep learning. *Nat. Methods* **20**, 1739–1747 (2023).
83. Emsley, P. et al. Features and development of Coot. *Acta Crystallogr. D Biol. Crystallogr.* **66**, 486–501 (2010).
84. Liebschner, D. et al. Macromolecular structure determination using X-rays, neutrons and electrons: recent developments in Phenix. *Acta Crystallogr. D Struct. Biol.* **75**, 861–877 (2019).
85. Williams, C. J. et al. MolProbity: more and better reference data for improved all-atom structure validation. *Protein Sci.* **27**, 293–315 (2018).
86. Pintilie, G. et al. Measurement of atom resolvability in cryo-EM maps with Q-scores. *Nat. Methods* **17**, 328–334 (2020).
87. Nawrocki, E. P. & Eddy, S. R. Infernal 1.1: 100-fold faster RNA homology searches. *Bioinformatics* **29**, 2933–2935 (2013).
88. Rivas, E., Clements, J. & Eddy, S. R. A statistical test for conserved RNA structure shows lack of evidence for structure in lncRNAs. *Nat. Methods* **14**, 45–48 (2017).
89. Pettersen, E. F. et al. UCSF Chimera—a visualization system for exploratory research and analysis. *J. Comput. Chem.* **25**, 1605–1612 (2004).

Acknowledgements

Cryo-EM data were collected on Can Cong at SKLB West China Cryo-EM Center and processed at SKLB Duyu High Performance Computing Center in West China Hospital of Sichuan University. This work was supported by National Key Research and Development Program of China (2022YFC2303700 to Z.S., 2021YFA1301900 to H.D.), Natural Science Foundation of China (NSFC 32222040 and 32070049 to Z.S., 32300030 to Y.Y. and 81970936 to D.H.) and the 1.3.5 Project for Disciplines Excellence of West China Hospital (ZYYC21006 to Z.S.).

Author contributions

Z.S. conceived the project. L.W. and C.Z. performed RNA preparation and gel electrophoresis. L.W., C.Z. and Y.Y. collected cryo-EM data. L.W., D.H. and Z.S. processed cryo-EM data. L.W., J.X., J.Z., S.S. and Z.S. generated RNA atomic coordinates. L.W., Z.H., Y.Y., X.C., H.D. and J.L. prepared figure illustrations. All authors contributed to the preparation of the manuscript.

Competing interests

The authors declare no competing interests.

Additional information

Extended data is available for this paper at <https://doi.org/10.1038/s41594-025-01484-x>.

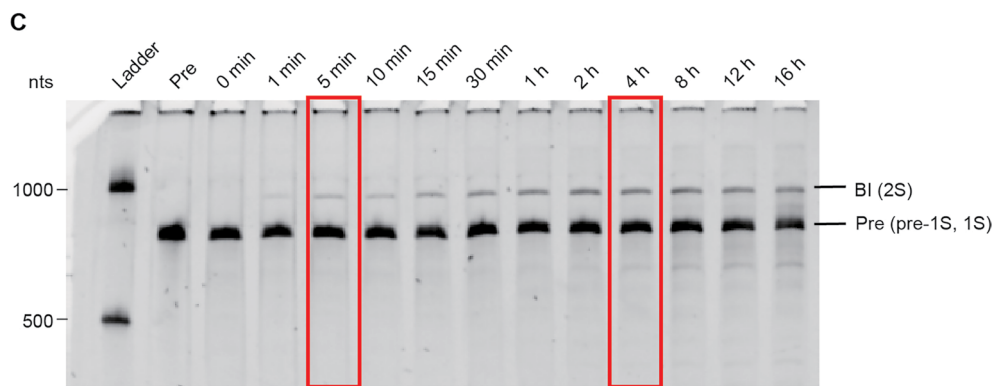
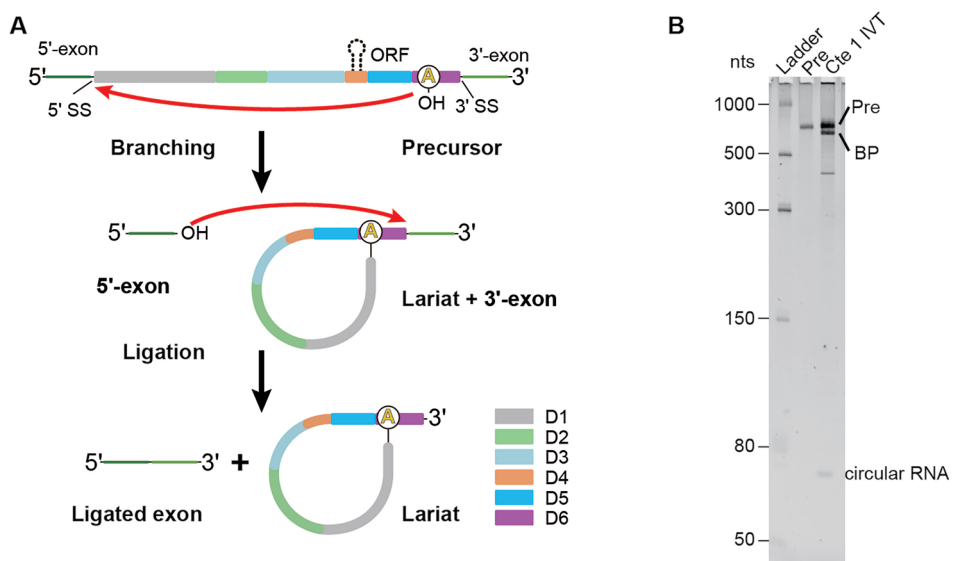
Supplementary information The online version contains supplementary material available at <https://doi.org/10.1038/s41594-025-01484-x>.

Correspondence and requests for materials should be addressed to Dingming Huang or Zhaoming Su.

Peer review information *Nature Structural & Molecular Biology* thanks the anonymous reviewers for their contribution to the peer review of

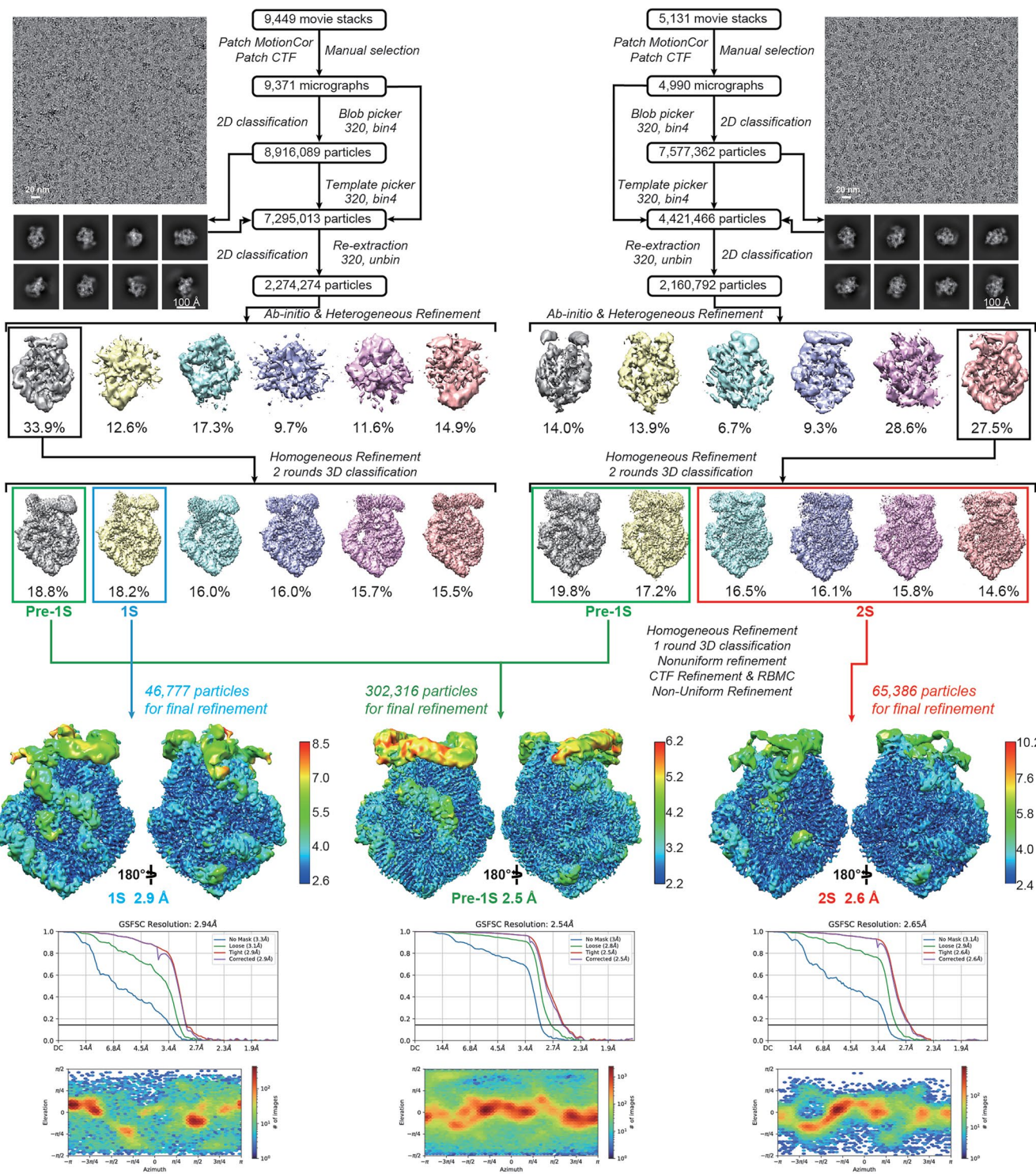
this work. Primary Handling Editor: Sara Osman, in collaboration with the *Nature Structural & Molecular Biology* team.

Reprints and permissions information is available at www.nature.com/reprints.

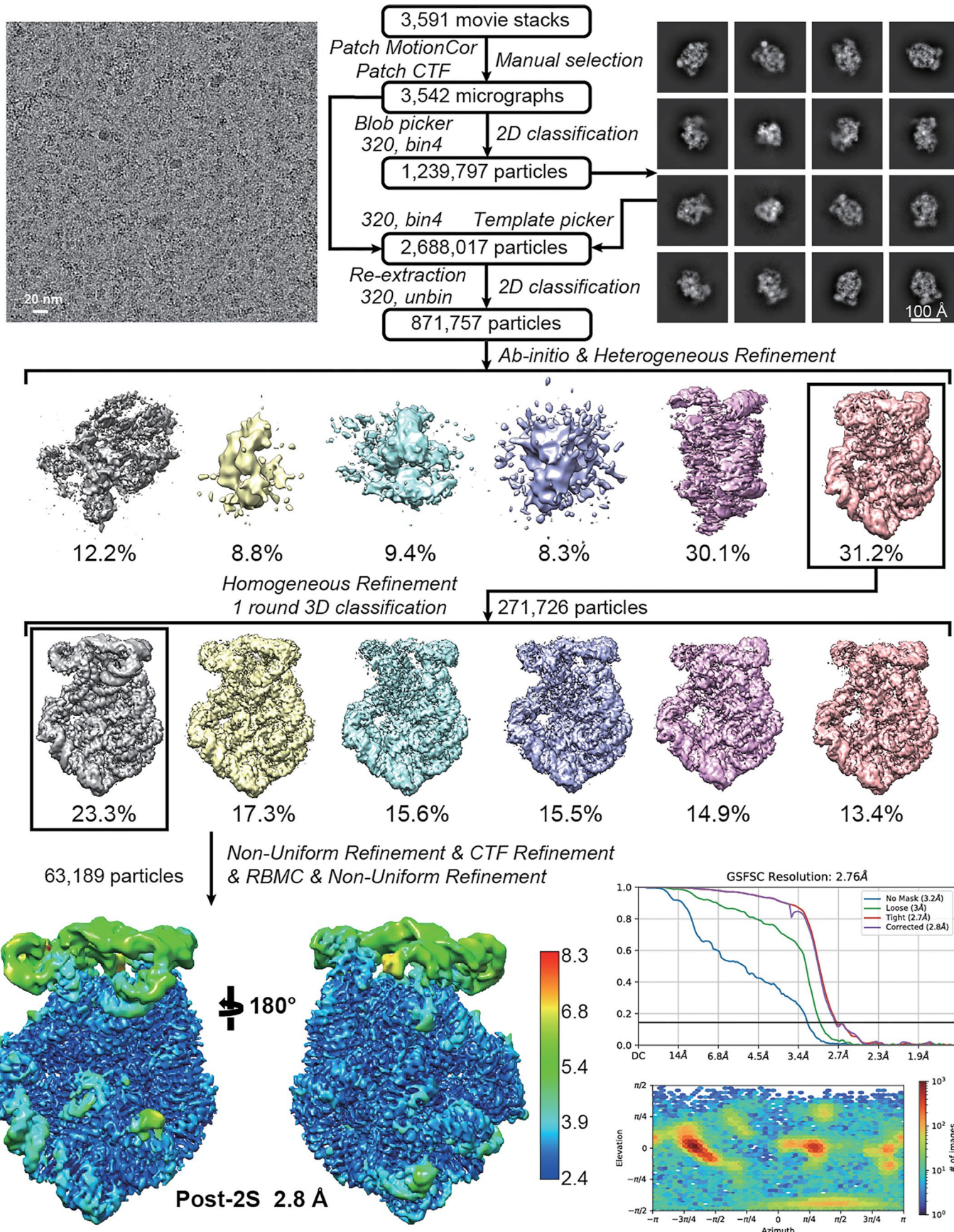


Extended Data Fig. 1 | *Cte1* CP intron back-splicing compared to canonical group II intron splicing. **a.** Schematic representation of canonical group II intron self-splicing to generate linear exon product. **b.** Representative denaturing gel electrophoresis of *Cte1* IVT product from three independent experiments

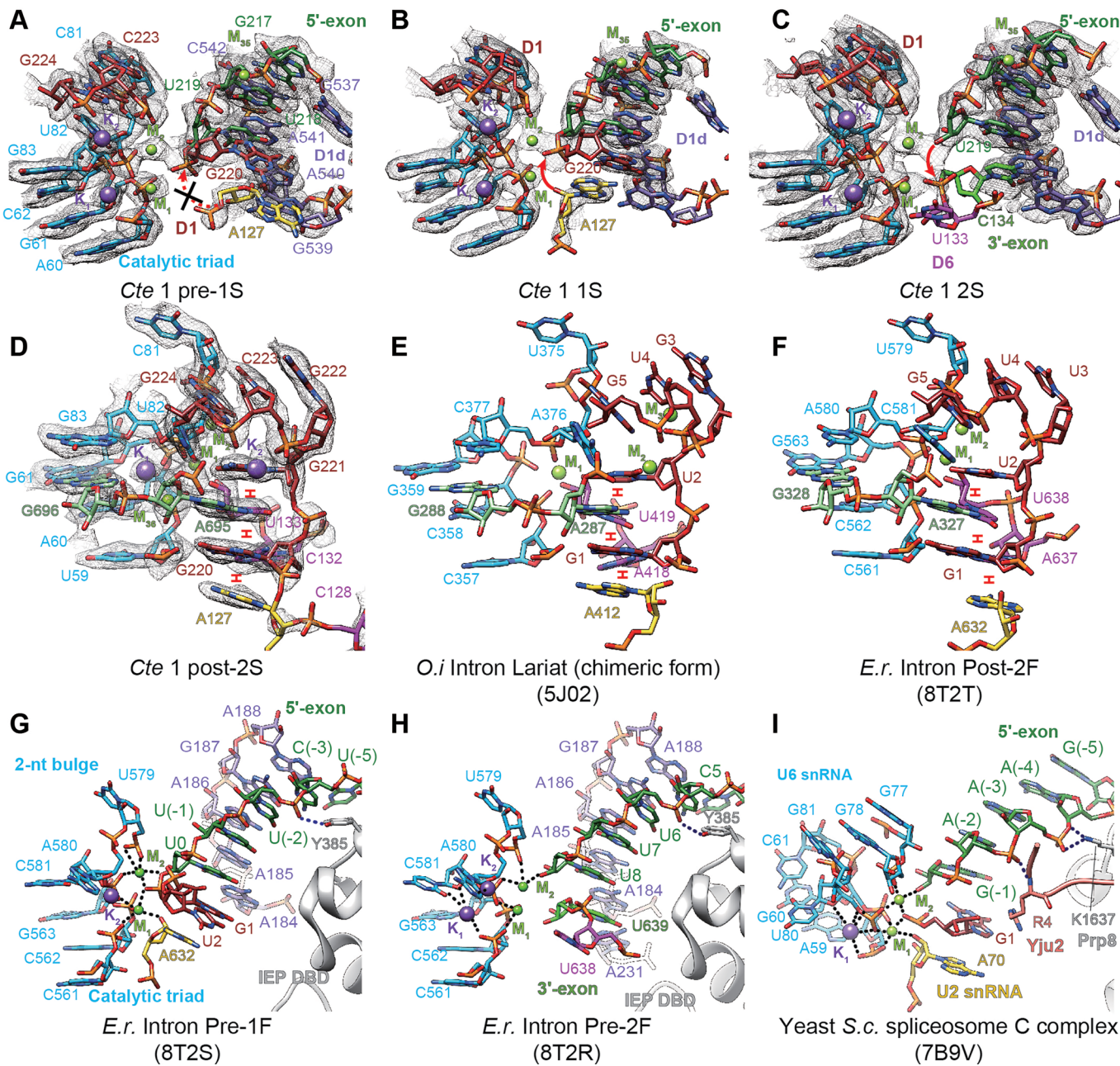
with consistent results. **c.** Representative denaturing gel electrophoresis of *Cte1* Pre RNA splicing in the presence of Ca^{2+} at different time points from three independent experiments with consistent results. Red boxes highlight samples subjected to cryo-EM analysis.



Extended Data Fig. 2 | Cryo-EM workflow for the Cte1 RNA splicing products. Cryo-EM data collection and processing of Cte1 RNA splicing products in the presence of Ca^{2+} at 5 minutes (left) and 4 hours (right).

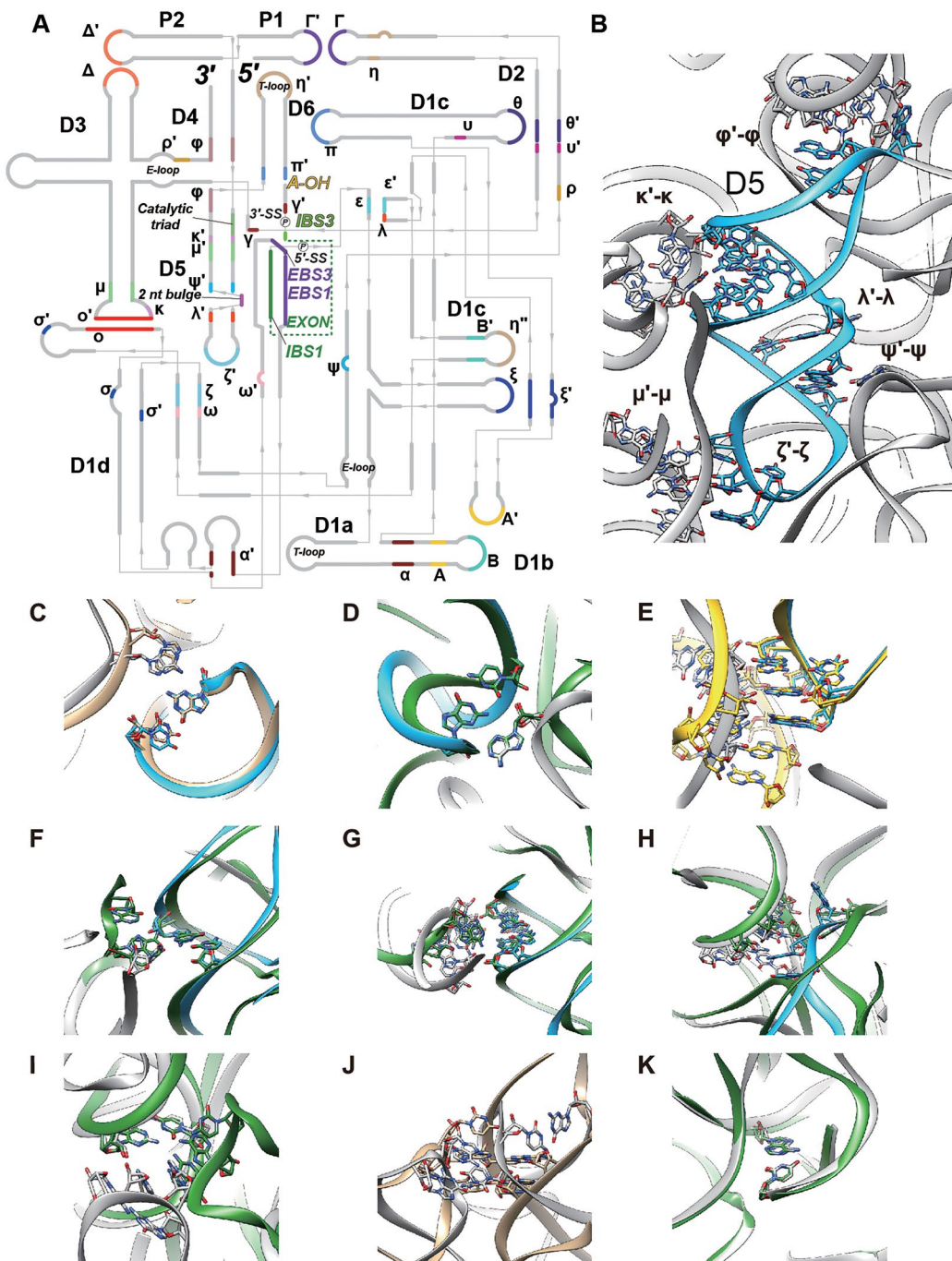


Extended Data Fig. 3 |Cryo-EM workflow for the *Cte1* IVT product. Cryo-EM data collection and processing of cotranscriptionally folded *Cte1* RNA splicing product directly after IVT.



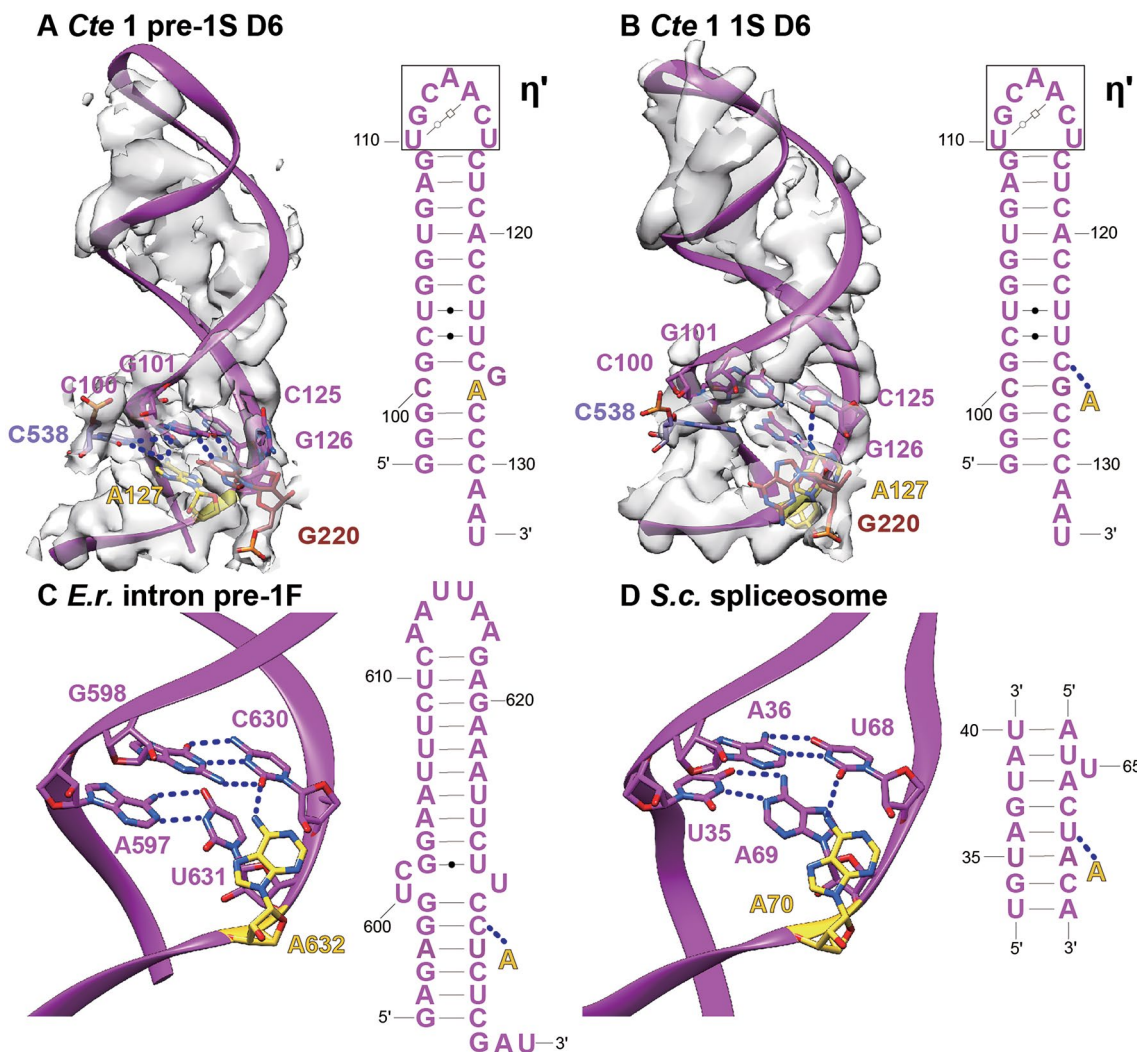
Extended Data Fig. 4 | The heteronuclear metal ion center in Cte 1 intron and comparison to canonical group II introns and spliceosome. **a-c.** The cryo-EM maps and models depicting the heteronuclear metal ion center showing EBS-IBS interactions in **a.** pre-1S, **b.** 1S, **c.** 2S, **d-f.** 3'-SS interaction network in **d.** post-2S, **e.** chimeric *O.i* intron lariat (5J02), **f.** *E.r*. intron RNP post-2F (8T2T), and homology

to **g.** *E.r*. intron RNP pre-1F (8T2S), **h.** *E.r*. intron RNP pre-2F (8T2R), **i.** yeast *S. cerevisiae* spliceosome C complex (7B9V). Black dashed lines indicate metal ion coordination, blue dashed lines indicate hydrogen bonds, arrows indicate nucleophilic attacks, and base stackings are highlighted in red.



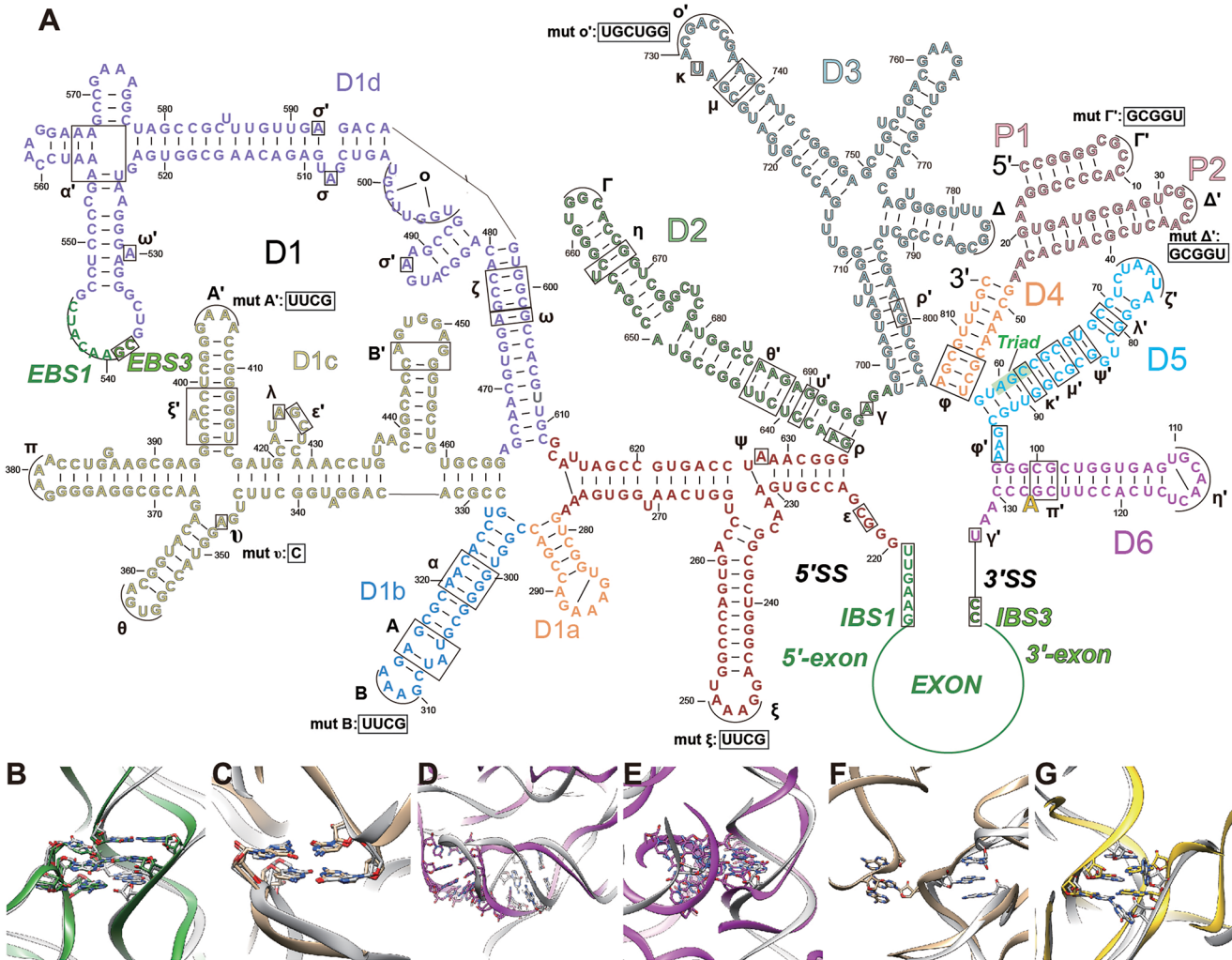
Extended Data Fig. 5 | Tertiary interactions of D5 and D6 in Cte1 intron compared to canonical group II introns. **a.** Projected secondary structure with designated tertiary interactions of Cte1 intron based on 3D structures. **b.** Tertiary interactions of D5 (cyan) with D1, D3 and D4 (gray). **c-h.** Cte1 (cyan and gray) tertiary interactions of **c.** ψ' - ψ compared to 6MEO (tan), **d.** λ' - λ compared

to 8T2T (forest green), **e.** ζ' - ζ compared to 4ROD (gold), **f.** κ' - κ compared to 8T2T, **g.** μ' - μ compared to 8T2T, **h.** φ' - φ compared to 8T2T. **i-k.** Cte1 (gray) tertiary interactions of **i.** π - π' compared to 8T2T (forest green), **j.** η - η' compared to 6MEO (tan), **k.** γ - γ' compared to 8T2T.


Extended Data Fig. 6 | Local shifts of bulged A between pre-1S and 1S.

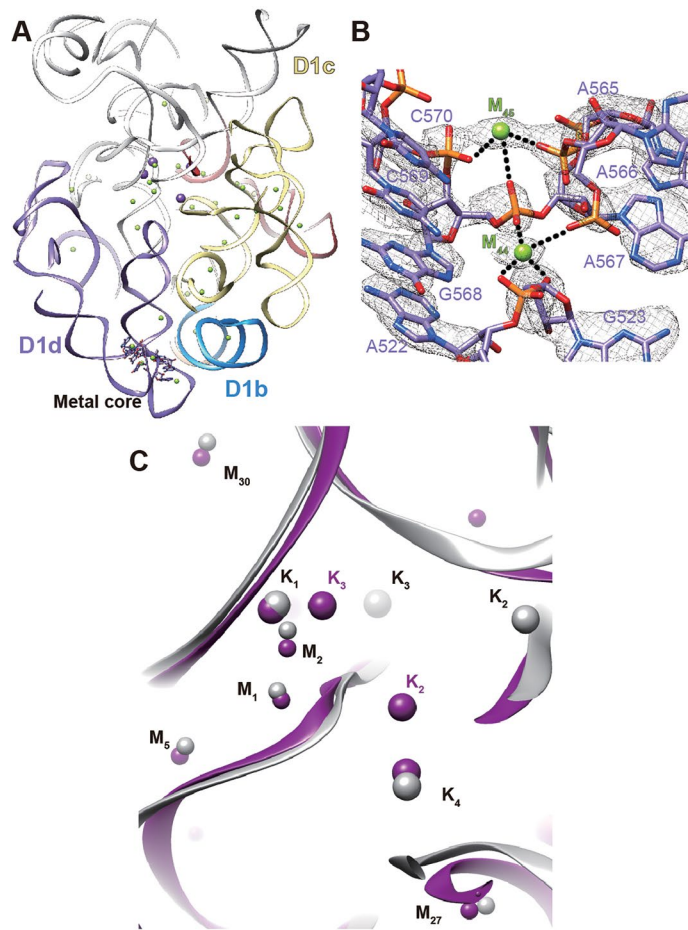
a. Secondary structure, cryo-EM density map and model of D6 showing a 2-nt bulge (G126 and A127) in pre-1S, in which two base triples C100-A127-C538 and G101-C125-G220 were formed. **b.** Secondary structure, cryo-EM density map and

model of D6 with bulged A127 interacting with G101-C125 in 1S. **c-d.** Analogous bulged A structure in **c.** canonical group II intron *E.r.* intron pre-1F (8T2S) and **d.** yeast *S.c.* spliceosome (7B9V). Blue dashed lines indicate hydrogen bonds.

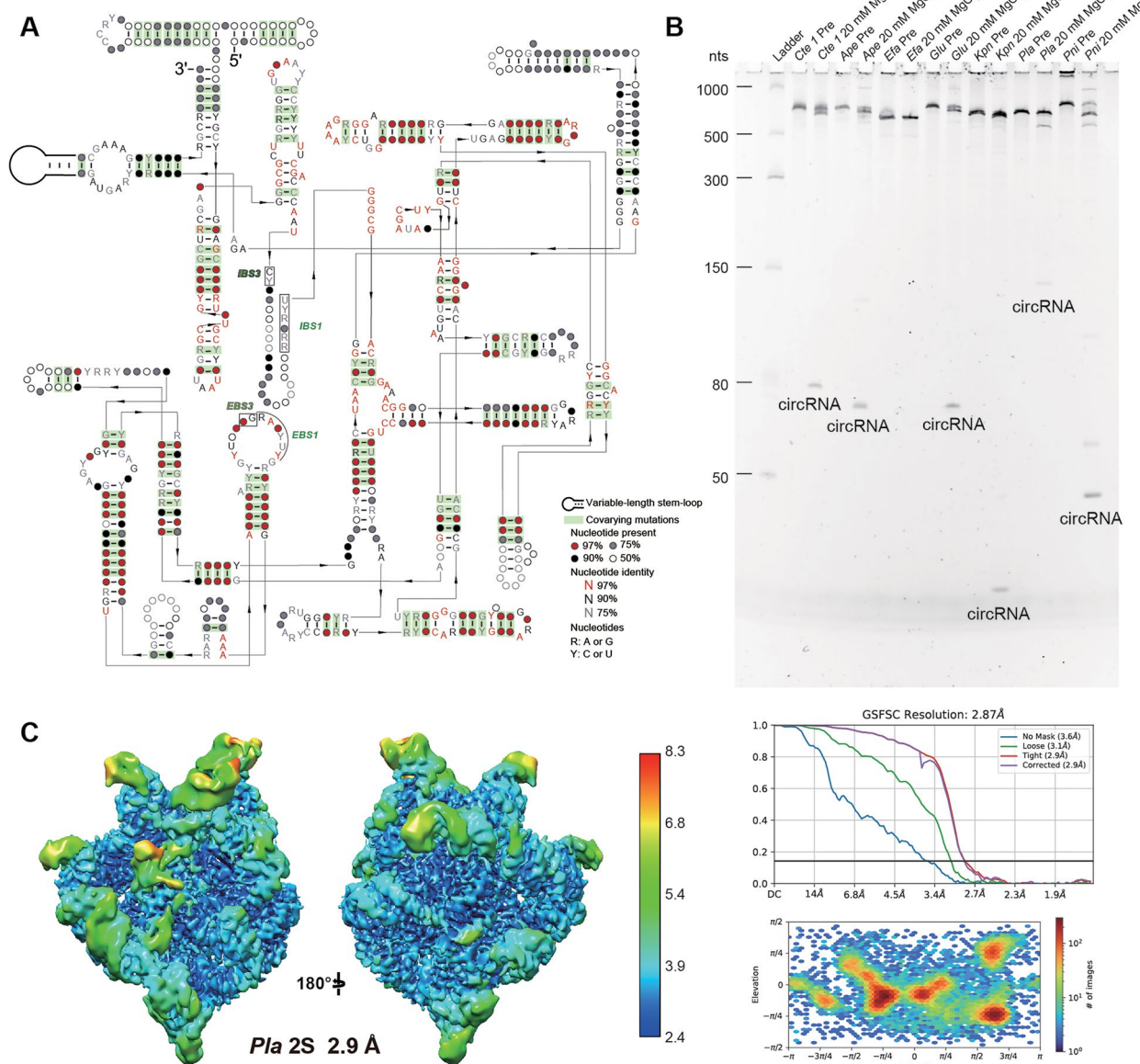


Extended Data Fig. 7 | Other tertiary interactions in Cte 1 intron compared to canonical group II introns. **a.** Projected secondary structures of Cte 1 intron. Mutations that disrupt novel tertiary interactions are denoted. Cte 1 intron (gray) tertiary interactions of **b.** θ - θ' compared to 8T2T, **c.** ε - ε' compared to 6MEO,

d. α - α' compared to 4E8K (magenta), **e.** ω - ω' compared to 4E8K, **f.** σ - σ' compared to 6MEO, **g.** ρ - ρ' compared to 4ROD (gold). Mutations that disrupt novel tertiary interactions are denoted in the secondary structure on top.

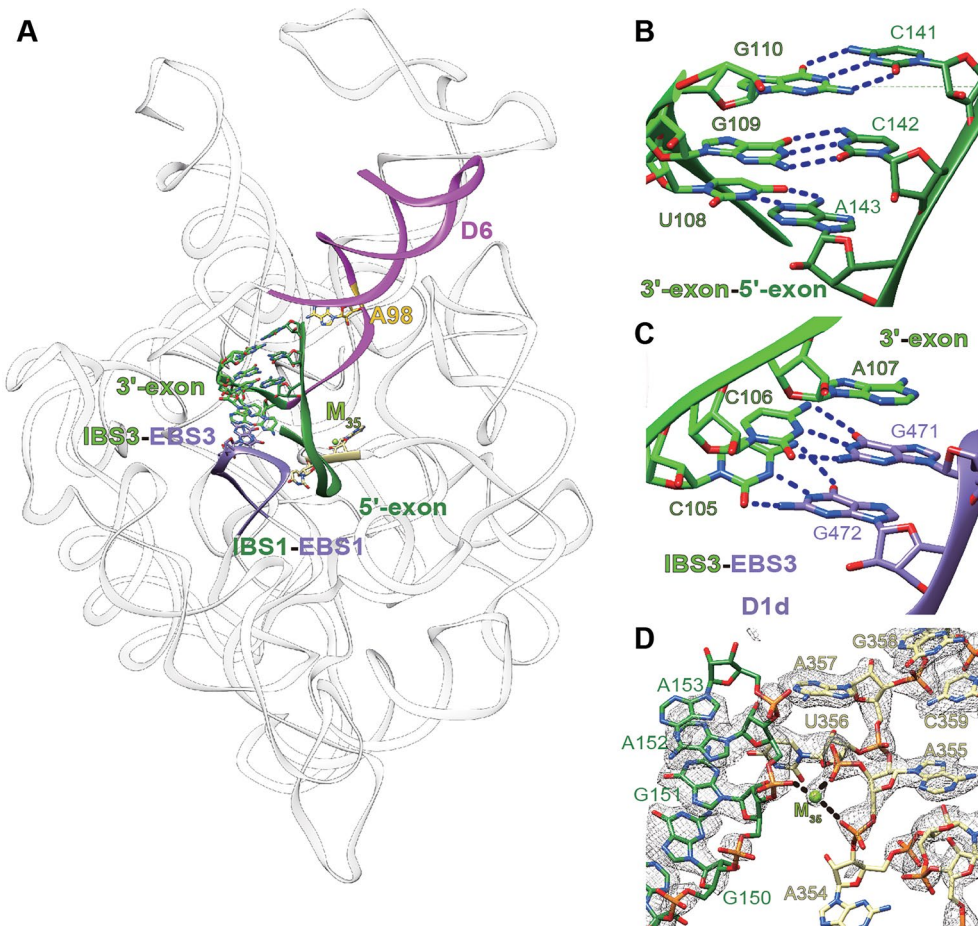


Extended Data Fig. 8 | Metal ion distribution in *Cte* 1 intron and comparison with *O. i.* group IIc intron (4E8Q). **a.** Metal ion distribution shows that most metal ions reside in D1 domain. **b.** The metal core in D1d domain. **c.** Comparison with *O. i.* group IIc intron reveals analogous metal ion-binding sites in the catalytic core. Black dashed lines indicate metal ion coordination.



Extended Data Fig. 9 | Covariation analysis facilitates discovery of novel CP group II introns in other bacteria. **a.** Consensus sequence and secondary structure model of CP group II intron, highlighting over one hundred covarying mutation pairs (green boxes). **b.** *In vitro* splicing assay demonstrates catalytic

activity of five newly identified CP group II introns from *Ape*, *Glu*, *Kpn*, *Pla*, and *Pni* with incubation at 37 °C for 30 minutes. This is a representative gel electrophoresis from three independent experiments with consistent results. **c.** 2.9 Å cryo-EM map of the *Pla* CP-GII intron.



Extended Data Fig. 10 | The *Pla* CP intron structure reveals conserved features as those in *Cte1* CP intron. **a.** The overall structure of *Pla* CP intron. **b.** 5'- and 3'-exon base-pairing interaction. **c.** The 2-bp EBS3-IBS3 interaction motif. **d.** M_{35} stabilizing the 5'-exon. Black and blue dashed lines indicate metal ion coordination and hydrogen bonds, respectively.

Reporting Summary

Nature Portfolio wishes to improve the reproducibility of the work that we publish. This form provides structure for consistency and transparency in reporting. For further information on Nature Portfolio policies, see our [Editorial Policies](#) and the [Editorial Policy Checklist](#).

Statistics

For all statistical analyses, confirm that the following items are present in the figure legend, table legend, main text, or Methods section.

n/a Confirmed

- The exact sample size (n) for each experimental group/condition, given as a discrete number and unit of measurement
- A statement on whether measurements were taken from distinct samples or whether the same sample was measured repeatedly
- The statistical test(s) used AND whether they are one- or two-sided
Only common tests should be described solely by name; describe more complex techniques in the Methods section.
- A description of all covariates tested
- A description of any assumptions or corrections, such as tests of normality and adjustment for multiple comparisons
- A full description of the statistical parameters including central tendency (e.g. means) or other basic estimates (e.g. regression coefficient) AND variation (e.g. standard deviation) or associated estimates of uncertainty (e.g. confidence intervals)
- For null hypothesis testing, the test statistic (e.g. F , t , r) with confidence intervals, effect sizes, degrees of freedom and P value noted
Give P values as exact values whenever suitable.
- For Bayesian analysis, information on the choice of priors and Markov chain Monte Carlo settings
- For hierarchical and complex designs, identification of the appropriate level for tests and full reporting of outcomes
- Estimates of effect sizes (e.g. Cohen's d , Pearson's r), indicating how they were calculated

Our web collection on [statistics for biologists](#) contains articles on many of the points above.

Software and code

Policy information about [availability of computer code](#)

Data collection EPU2.9 (Thermofisher)

Data analysis

All software are publicly accessible.
 Data processing: CryoSPARC v4.4.1.
 Visualization: Chimera 1.16, ChimeraX 1.6.
 Model refinement and validation: Coot 0.9.8, Phenix 1.15, Molprobity 4.5.1, Q-score, autoDRRAFTER, CryoREAD v8.2.
 Covariation analysis: Infernal v1.1.4, R-scape.
 Secondary structure drawing: Adobe Illustrator 2020 and Adobe Premiere Pro 2020.
 Statistic figure drawing and plotting: GraphPad PRISM 10.0.

For manuscripts utilizing custom algorithms or software that are central to the research but not yet described in published literature, software must be made available to editors and reviewers. We strongly encourage code deposition in a community repository (e.g. GitHub). See the Nature Portfolio [guidelines for submitting code & software](#) for further information.

Data

Policy information about [availability of data](#)

All manuscripts must include a [data availability statement](#). This statement should provide the following information, where applicable:

- Accession codes, unique identifiers, or web links for publicly available datasets
- A description of any restrictions on data availability
- For clinical datasets or third party data, please ensure that the statement adheres to our [policy](#)

The cryo-EM maps and associated atomic coordinate models of Comamonas testosteroni KF-1 CP-group II intron pre-1S, 1S, 2S, and post-2S and Paracandidimonas lacteal CP-group II intron 2S have been deposited in the wwPDB OneDep System under EMD accession codes of EMD-38649, EMD-38647, EMD-38648, EMD-38646 and EMD-60833 and PDB ID codes of 8XTS, 8XTQ, 8XTR, 8XTP and 9IS7, respectively.

NCBI nucleotide dataset (<https://ftp.ncbi.nlm.nih.gov/blast/db/FASTA/nt.gz>) is used for comparative analysis. Full-length WT and mutated Comamonas testosteroni KF-1 sequences were used according to NCBI (GenBank: NZ_AAUJO20000001.1). Full-length WT Paracandidimonas lactea strain Q2-2 sequence was used according to NCBI (GenBank: NZ_JAJJOZ000000000.1)

Research involving human participants, their data, or biological material

Policy information about studies with [human participants or human data](#). See also policy information about [sex, gender \(identity/presentation\), and sexual orientation](#) and [race, ethnicity and racism](#).

Reporting on sex and gender	N/A
Reporting on race, ethnicity, or other socially relevant groupings	N/A
Population characteristics	N/A
Recruitment	N/A
Ethics oversight	N/A

Note that full information on the approval of the study protocol must also be provided in the manuscript.

Field-specific reporting

Please select the one below that is the best fit for your research. If you are not sure, read the appropriate sections before making your selection.

Life sciences Behavioural & social sciences Ecological, evolutionary & environmental sciences

For a reference copy of the document with all sections, see nature.com/documents/nr-reporting-summary-flat.pdf

Life sciences study design

All studies must disclose on these points even when the disclosure is negative.

Sample size	In order to resolve the conformational dynamics of Cte 1 intron, we collected a total of 19,649 movie stacks. Four cryo-EM structures were resolved, including pre-1S of 302,316 particles at 2.5 Å resolution, 1S of 46,777 particles at 2.9 Å resolution, 2S of 65,386 particles at 2.6 Å resolution, and post-2S of 63,189 particles at 2.8 Å resolution. We collected 1,478 movie stacks of Pla IVT product and resolved a cryo-EM structure of 2S (33,739 particles) at 2.9 Å resolution. The cryo-EM sample size was not predetermined and the sample sizes are sufficient based on the achieved resolutions. Sample size of gel analysis for measuring the catalytic activity of Cte 1 intron self-splicing was three (n=3). The sample size was not predetermined and the sample size is sufficient for statistics analysis
Data exclusions	For cryo-EM analysis, particles that did not belong to the classes of interest or have poor qualities based on well established cryo-EM principles were excluded after multiple rounds of 2D and 3D classifications.
Replication	The standard single-particle cryo-EM workflow does not involve replication, because each dataset normally involves tens of thousands of micrographs collected in the same manner..Similar tasks like 2D and 3D classifications might be repeated but input and parameters were usually different. Each biochemical experiment was performed 3 times independently. All replicate experiments were successful.
Randomization	No grouping required for our studies.
Blinding	Blinding was not necessary for either structure determination or catalytic activity measurements, because there was no expected outcome for either experiment.

Reporting for specific materials, systems and methods

We require information from authors about some types of materials, experimental systems and methods used in many studies. Here, indicate whether each material, system or method listed is relevant to your study. If you are not sure if a list item applies to your research, read the appropriate section before selecting a response.

Materials & experimental systems

n/a	Involved in the study
<input checked="" type="checkbox"/>	Antibodies
<input checked="" type="checkbox"/>	Eukaryotic cell lines
<input checked="" type="checkbox"/>	Palaeontology and archaeology
<input checked="" type="checkbox"/>	Animals and other organisms
<input checked="" type="checkbox"/>	Clinical data
<input checked="" type="checkbox"/>	Dual use research of concern
<input checked="" type="checkbox"/>	Plants

Methods

n/a	Involved in the study
<input checked="" type="checkbox"/>	ChIP-seq
<input checked="" type="checkbox"/>	Flow cytometry
<input checked="" type="checkbox"/>	MRI-based neuroimaging

Plants

Seed stocks

N/A

Novel plant genotypes

N/A

Authentication

N/A